

# Recent Advances on High-Speed and Holographic Two-Photon Direct Laser Writing

Antonio Balena,\* Marco Bianco,\* Ferruccio Pisanello,\* and Massimo De Vittorio\*

Two-Photon Lithography, thanks to its very high sub-diffraction resolution, has become the lithographic technique par excellence in applications requiring small feature sizes and complex 3D patterning. Despite this, the fabrication times required for extended structures remain much longer than those of other competing techniques (UV mask lithography, nanoimprinting, etc.). Its low throughput prevents its wide adoption in industrial applications. To increase it, over the years different solutions have been proposed, although their usage is difficult to generalize and may be limited depending on the specific application. A promising strategy to further increase the throughput of Two-Photon Lithography, opening a concrete window for its adoption in industry, lies in its combination with holography approaches: in this way it is possible to generate dozens of foci from a single laser beam, thus parallelizing the fabrication of periodic structures, or to engineer the intensity distribution on the writing plane in a complex way, obtaining 3D microstructures with a single exposure. Here, the fundamental concepts behind high-speed Two-Photon Lithography and its combination with holography are discussed, and the literary production of recent years that exploits such techniques is reviewed, and contextualized according to the topic covered.

of the Two-Photon Photopolymerization (TPP) process. This was first demonstrated in 1965 by Pao and Rentzepis,<sup>[3]</sup> and it became the go-to option when small feature size and complex 3D structuring are required.<sup>[4,5]</sup> Starting from the late nineties, thanks to the work of Maruo et al. (1997),<sup>[6]</sup> TPP became a lithographic technology (Two-Photon Lithography, TPL) complementing other approaches based on UV light or electron beams, and nowadays finds countless applications in different fields, spanning from optics and photonics<sup>[7–9]</sup> to microfluidics,<sup>[10]</sup> bioengineering,<sup>[11–13]</sup> and even devices for neuroscience.<sup>[14]</sup> TPL combines the versatility of macroscopic 3D printing approaches with the high resolution of conventional planar microfabrication techniques, such as UV photolithography. Albeit the resolution of the writing process depends on a series of different aspects (wavelength, light intensity, objective lens, optical dose, etc.), TPL allows to circumvent the diffraction limit of the focused beam providing high resolution, with features below 100 nm frequently reported in the literature.<sup>[15]</sup>

## 1. Introduction

Since the pioneering theoretical, conceptualization,<sup>[1]</sup> and experimental demonstration<sup>[2]</sup> of Two-Photon Absorption (TPA), well aware of its potential, the scientific community has devoted relentless engagement on the development and exploitation

of the Two-Photon Photopolymerization (TPP) process. This was first demonstrated in 1965 by Pao and Rentzepis,<sup>[3]</sup> and it became the go-to option when small feature size and complex 3D structuring are required.<sup>[4,5]</sup> Starting from the late nineties, thanks to the work of Maruo et al. (1997),<sup>[6]</sup> TPP became a lithographic technology (Two-Photon Lithography, TPL) complementing other approaches based on UV light or electron beams, and nowadays finds countless applications in different fields, spanning from optics and photonics<sup>[7–9]</sup> to microfluidics,<sup>[10]</sup> bioengineering,<sup>[11–13]</sup> and even devices for neuroscience.<sup>[14]</sup> TPL combines the versatility of macroscopic 3D printing approaches with the high resolution of conventional planar microfabrication techniques, such as UV photolithography. Albeit the resolution of the writing process depends on a series of different aspects (wavelength, light intensity, objective lens, optical dose, etc.), TPL allows to circumvent the diffraction limit of the focused beam providing high resolution, with features below 100 nm frequently reported in the literature.<sup>[15]</sup>

Despite the unquestionable versatility of TPL, due to its intrinsic characteristics, various aspects affect the speed and its overall throughput in wide-area fabrication. TPA is indeed characterized by an absorption cross section several orders of magnitude smaller than its one-photon counterpart, being a third-order non-linear process, with the probability to observe TPA being proportional to the square of light intensity. Thus, high-intensity and ultrafast pulsed lasers are required for obtaining TPA in photoresists, enhancing the probability of the simultaneous absorption of two photons in a restricted volume, to initiate a localized chemical chain reaction which leads to the polymerization of the resin inside the focal volume (a volume-pixel or voxel), without light absorption outside of it.

From an exquisitely applicative point of view, this means that only a small volume in correspondence with the focus can be polymerized and that the polymerization of a wide area, as well as a complex 3D geometry, requires the exposure and the stitching of multiple voxels in a serial fashion. Consequently, the fabrication time scales with the volume of the processed pattern and the resolution of the system, and the realization of a single structure may require from several hours up to some days depending on the dimension of the object, the filling factor, and the finesse of the features. This, in turn strongly

A. Balena, M. Bianco, F. Pisanello, M. De Vittorio  
Center for Biomolecular Nanotechnologies  
Istituto Italiano di Tecnologia (IIT)  
Via Barsanti 14, Arnesano, 73010 Lecce, Italy  
E-mail: antonio.balena@iit.it; marco.bianco@iit.it;  
ferruccio.pisanello@iit.it; massimo.devittorio@iit.it  
M. De Vittorio  
Dipartimento di Ingegneria dell'Innovazione  
Università del Salento  
Via per Monteroni, 73100 Lecce, Italy

 The ORCID identification number(s) for the author(s) of this article can be found under <https://doi.org/10.1002/adfm.202211773>.

© 2023 The Authors. Advanced Functional Materials published by Wiley-VCH GmbH. This is an open access article under the terms of the Creative Commons Attribution-NonCommercial-NoDerivs License, which permits use and distribution in any medium, provided the original work is properly cited, the use is non-commercial and no modifications or adaptations are made.

DOI: 10.1002/adfm.202211773

affects the throughput, particularly if compared to one-photon absorption-based techniques, in which areas of the order of several mm<sup>2</sup>, or even cm<sup>2</sup>, can be patterned at once, thus finding application in mass production.

Efforts made through the years to mitigate, or to suppress these differences, have followed two main perimeters of action: i) optimizing the chemical properties of the photoresists, ii) circumventing the physical limitations of the optical system employed for the polymerization. As an example of recent works on the optimization of the photoresist's chemical properties, Zhang and collaborators proposed a high-efficiency photo-initiator with a conjugated A- $\pi$ -D- $\pi$ -A structure of phenothiazine and carbazole derivatives,<sup>[16]</sup> achieving a writing speed of 14 mm s<sup>-1</sup>, while Li and coworkers showed the synthesis of a series of  $\pi$ -extended benzophenone photoinitiators,<sup>[17]</sup> which allowed to reach a writing speed of 100 mm s<sup>-1</sup>. Liao et al.<sup>[18]</sup> and Spadaccini et al.<sup>[19]</sup> have provided comprehensive reviews on materials and challenges for developing the next generation of TPL photoresists.

Optimization of TPA cross sections has been accompanied by intensive research activity on how to structure the phase profile of the writing light beam to increase TPL throughput. Latest developments can be categorized as: i) static approaches, relying on the use of static phase masks or patterned optical elements inserted along the optical path, most of which are in transmission configuration, and ii) dynamic approaches, based on wave-front shaping using electronically controlled phase modulation elements, such as Spatial Light Modulators (SLMs) or digital micromirror devices (DMDs), dynamically projecting Computer Generated Holograms (CGHs) during the writing process.

This review is structured into four main sections: i) in Section 2 the general aspects of TPP are introduced along with a brief theoretical overview, and the introduction of some figures of merit (average power, exposure time, and optical dosage) which determine the size of the polymerizing voxel, defining the resolution of the process. In this context, we review the approaches reported in literature to improve the resolution of TPL by exploiting custom photoresists with added radical quenchers, or Stimulated Emission Depletion-like (STED) techniques. ii) Section 3 discusses the factors defining the upper limit of the writing speed in TPL, including the physical properties of the photoresist, the incurrence of thermal effects, and the employed scanning strategies. We also review the most employed conventional parallelization techniques, which combine TPL with transparency masks, patterned optical elements, or replication molds. iii) Section 4 is devoted to the dynamical approaches that combine TPL with the advantages offered by holographic techniques. A short theoretical introduction on holography and phase shaping is presented, as well as the optical arrangement required for their physical implementation, and the different algorithms for CGH generation. Second, we review the recent advances on two well-distinct topics, which are the improvement in overall throughput by generation of multi-foci on the writing plane through CGH gratings and the use of phase modulation for beam shaping, achieving complex 3D structuration of the voxel or compensation of optical aberrations. iv) The last section—Section 5—reviews how these techniques have been exploited in different application fields, such as optics and photonics, microfluidics, and microactuators. The aim of this review is to

offer an extensive viewpoint on how the holographic approaches and more conventional parallelization techniques combined with TPL are allowing for a substantial development of TPL applications, which could achieve the potential of becoming a fast, scalable, and reliable manufacturing technique, not only limited to laboratory and prototyping frameworks.

## 2. Two-Photon Direct Laser Writing: Basic Principles and Definitions

TPL sub-diffraction resolution allows the fabrication of actual 3D structures in volumes that can reach even cubic millimeters with sub-micrometric features. In this Section, we briefly review the principles of TPL, from the basic mechanism of TPA to the propagation of the photo-induced chemical reaction which leads to the cross-linking of monomers inside the resin. We also discuss how the writing parameters, the optical system, and the typology of photoresists can influence shape and size of the voxel and, in general, the resolution of the process, along with the most frequently employed solutions to improve it.

### 2.1. General Aspects and Theoretical Overview

TPP is based on TPA and takes advantage of the simultaneous absorption of a pair of photons to drive an electronic transition in a molecule. Considering an electronic transition from the ground state  $|g\rangle$  to the excited state  $|f\rangle$  in a two-level system (Figure 1A), the energy gap is given by  $E_{g \rightarrow f} = E_f - E_g = h\nu_{gf}$ . In TPP, the energy of each photon  $E_{ph} = h\nu_{ph} = \frac{h\nu_{gf}}{2}$  is out of resonance with the transition, but it creates a non-stationary virtual state which exists for a time in the order of femtoseconds.<sup>[20]</sup> If the second photon with energy  $E_{ph}$  impinges with a time delay shorter than the virtual state lifetime, it can be absorbed inducing the transition to the final excited state  $|f\rangle$ . The light-matter energy change per unit volume and per unit time is:<sup>[21]</sup>

$$\frac{dW}{dt} \propto \text{Im}[\chi^{(3)}]I^2 \quad (1)$$

Where  $\chi^{(3)}$  is the third-order susceptibility tensor of the material, and  $I$  [W cm<sup>-2</sup>] represents the intensity of the excitation beam. Given the dependence from  $\chi^{(3)}$ , TPA is a third-order non-linear process. TPA cross section is typically several orders of magnitude smaller than the Single-Photon Absorption (SPA) one,<sup>[20]</sup> since two photons need to be very close in time and space to generate a transition. Femtosecond pulsed lasers tunable in the Near Infrared (NIR) regime, such as solid-state Ti: Sapphire oscillators, are the most used light sources in applications exploiting TPA, but in recent years less expensive femtosecond fiber lasers<sup>[22,23]</sup> were also employed, which however have the constraint of working at a fixed NIR wavelength (usually 780 nm). Their characteristics are optimal for TPA as i) the simultaneous absorption of two NIR photons can overcome the transition energy gap of molecules typically excitable in the UV spectrum, ii) the temporal width of the pulses, in the order of 100 fs with a repetition rate of 80 MHz, is com-

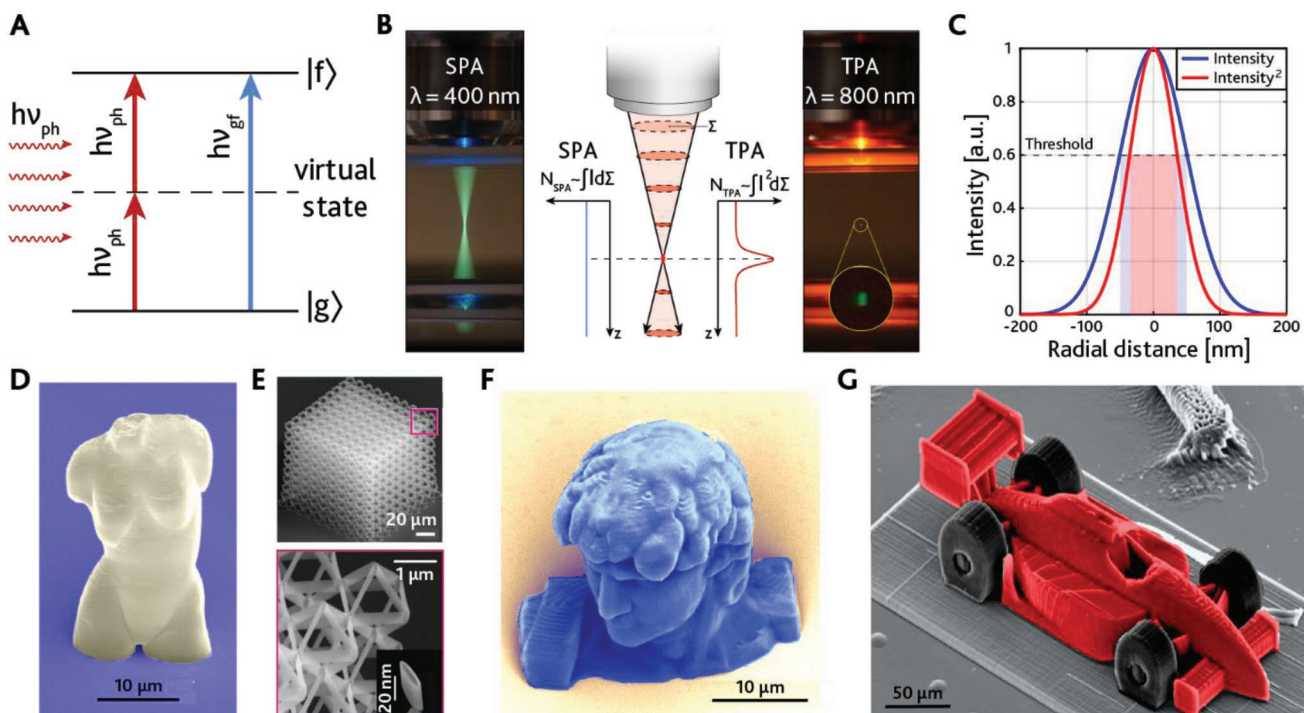
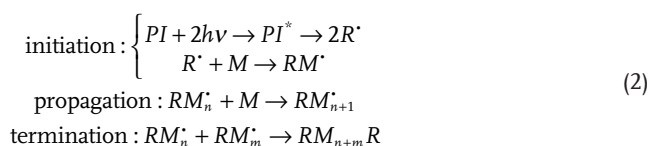


**Figure 1.** A) Energy level diagram of the  $|g\rangle \rightarrow |f\rangle$  transition. B) Fluorescence generated in a solution by SPA (left) and by TPA (right). The number of excited molecules in each transverse cross section of the laser beam does not depend on the axial position for SPA, but it is tightly peaked in the focus of the beam for TPA (center). C) Distribution of the light intensity (blue) and squared intensity (red) in the focus of a Gaussian beam. The polymerization process takes place in the spatial region where the intensity reaches the threshold, so the polymerized region for a TPA process (red area) is smaller than polymerized region for a SPA process (blue area). D–G) Roundup of several 3D micro-objects fabricated via TPL. D) SEM (Scanning Electron Microscope) micrograph of Venus fabricated by TPP. Adapted with permission.<sup>[34]</sup> Copyright 2003, Optical Society of America. E) SEM micrograph of a hollow titanium nitride (TiN) nanolattice. The skeleton of the structure was fabricated with TPL; conformal deposition of TiN was performed with atomic layer deposition. Adapted with permission.<sup>[35]</sup> Copyright 2013, The Authors, published by Springer Nature. F) Bust of Michelangelo's David. Adapted with permission.<sup>[36]</sup> Copyright 2015, Society of Photo-Optical Instrumentation Engineers (SPIE). G) 3D racecar fabricated with TPL. Adapted with permission.<sup>[37]</sup> Copyright 2013, American Chemical Society.

parable with the lifetime of the virtual state, iii) the ultrafast pulses allow achieving the high peak intensity required for TPA at a relatively low average laser power. Those lasers are widely employed for different kinds of laser processing applications, such as two-photon imaging,<sup>[24,25]</sup> ablation of metals,<sup>[26]</sup> chemical photoreduction,<sup>[27]</sup> and, of course, TPL.

In TPL the beam is tightly focused in a photo-sensitive resin (also called photoresist) to initiate the polymerization process. A photoresist is defined as positive-tone or negative-tone whether its solubility increases or decreases upon light exposure: in positive resists, the irradiated part is not polymerized and can be removed by using common solvents like Isopropyl Alcohol or Ethanol during the development step; conversely, in negative-tone resists only the exposed part remains on the substrate after the development.<sup>[28]</sup> Negative-tone resists are the most employed for the direct laser writing of 3D complex structures, or small structures with fine features. In contrast, positive-tone resists are commonly used in top-down approaches, where small features such as lines and dots need to be translated into the substrate or to define masks for 2D UV photolithography and electron-beam lithography. Moreover, positive resists found large applications in the fabrication of integrated circuits or conductor paths for lab-on-chip given the reduced shrinkage, the more economic processing, and the possibility to remove the resist

in case of deficient lithography. Some examples are reported in the works of Heiskanen et al.<sup>[29]</sup> and Braun et al.,<sup>[30]</sup> in which a positive-tone resist is exposed and removed after the development, then a deposition of metal followed by the lift-off process of the unexposed resist allows the realization of periodic arrays of metallic nano- and micro-structures. Although resins for TPP are composed of a multitude of chemical compounds, the crucial components are the photo-initiator and the monomers. In radical polymerization,<sup>[31]</sup> the photo-initiator absorbs two photons creating a free radical, a neutral molecule with an unpaired valence electron, which is highly chemically reactive. Free radicals bond to a monomer that becomes a radical in turn, creating a chain reaction that propagates in the solution, cross-linking the monomer to form a long polymeric chain. The process eventually stops when two free radicals bond to each other, or by the depletion of monomers caused by the action of inhibitors. The main steps of process are schematized in the following model, developed by Maruo et al.:<sup>[6]</sup>



where  $PI$  is a photo-initiator molecule,  $h\nu$  is a photon,  $R$  is a radical molecule,  $M$  is a monomer, and  $M_n$  is a polymeric chain of  $n$  monomers, and the superscript dot indicates the presence of an unpaired electron.<sup>[32]</sup> The vast majority of commercially available photoresists have negligible linear absorption in the red and NIR region of the spectrum, allowing the laser beam to penetrate deeply inside the material, triggering the polymerization process only inside the focal volume, by virtue of the quadratic intensity dependence of TPA.

Conversely to SPA, in which absorption may occur outside of the focal volume (Figure 1B), in TPA the number of excited molecules ( $N_{TPA}$ ) is inversely proportional to the transversal cross section of the laser beam, thus strongly increases in the focus of the beam.<sup>[33]</sup> The power of the laser beam can be precisely controlled to exceed the polymerization threshold only in this spatial region (Figure 1C). During the writing process, the focus position is typically moved on a plane to expose specific domains of the resist, then the objective lens is moved upwards to write the next layer of the structure. The sample is eventually developed to wash away the soluble unpolymerized resist, while the exposed resist remains anchored to the substrate, resulting in the formation of 3D micro-objects (Figure 1D–G).

## 2.2. Resolution of TPP

The non-linear absorption behavior of TPP allows to circumvent Abbe's law of diffraction,<sup>[38]</sup> often enabling a writing resolution, or the minimum lateral and axial distance at which two adjacent features can be patterned without any overlap, below 100 nm.<sup>[39–43]</sup> Moreover, several factors can contribute to the decreasing of the voxel size below Abbe's diffraction limit. Chemical non-linearity is a key factor to be considered because of the quenching processes that follow a photo-excitation event, there is an intensity threshold below which the photo-polymerization process cannot be sustained.<sup>[5,44]</sup> Acting on the concentration of photo-initiators or on the average power of the laser beam, it is therefore, possible to exceed the polymerization threshold only in a sub-volume inside the focal spot, that can be smaller than the laser focus, circumventing the limit of Abbe's law. Along with that, the effective size of the voxel is influenced by several other factors (concentration of inhibitors, radical quantum yield, viscosity, etc.). It is possible to estimate the radial and axial dimensions of the elliptical voxel (Figure 2A) with a simplified model, also referred as linear-exposure model.<sup>[34]</sup> According to this model, the lateral size of the voxel  $d(P,t)$  and its axial length  $l(P,t)$ , as a function of the laser power  $P$  and time  $t$ , can be evaluated as:

$$d(P,t) = \omega_0 \ln \left( \frac{\delta I_0^2 n \tau}{C} \right)^{1/2} \quad (3)$$

$$l(P,t) = 2z_R \left[ \left( \frac{\delta I_0^2 n \tau}{C} \right)^{\frac{1}{2}} - 1 \right]^{1/2} \quad (4)$$

Where  $\omega_0$  and  $z_R$  are, respectively, the waist and the Rayleigh length of the laser beam, which linearly depend on the laser wavelength  $\lambda$ ,  $I_0$  is its intensity at the center of the focal plane,  $\tau$

is the temporal pulse-width,  $n$  is the number of pulses,  $\delta$  is the TPA cross section of the PI molecule, and  $C$  is a constant that depends on the initial PI concentration and on the polymerization threshold. The computation of these functions for some typical writing parameters is reported in Figure 2B. From Equations 3 and 4, the volume of the voxel  $V \propto d^2 l$ , is proportional to the third power of the wavelength  $\lambda^3$  and increases with the exposure time  $t$  and average laser power  $P$ .

Conversely, it has been shown by Heiskanen et al.<sup>[29]</sup> that increasing the writing speed  $v$  improves the resolution of the process according to:

$$w = \omega_0 \sqrt{\ln \left( \frac{\sqrt{\pi} \delta I_0^2 \omega_0}{2 C v} \right)} \quad (5)$$

where  $w$  is the resulting linewidth. However, this simplified model does not consider the effect of the increased temperature due to thermal accumulation processes, as well as leaving out the effect of the viscosity of the resin. Indeed, modeling viscosity in a realistic model poses a great challenge, since between the voxel and its surroundings there is not a sharp division of solid and liquid phases, as this quantity is not constant during the polymerization reaction.<sup>[45]</sup> Sun et al. showed that the voxel aspect ratio  $\alpha = l/d$  changes substantially if the ratio of power and exposure time is changed while keeping constant the product of the quantities, or the optical dosage  $D$ .<sup>[46]</sup> To explain this, they proposed two different mechanisms (Figure 2C): the first, defined as focal spot duplication, depends on the Point Spread Function (PSF) of the laser beam, causing the voxel to grow non-homogeneously for increasing  $P$ , thus increasing  $\alpha$ . The second mechanism, defined voxel growth, is related to the presence of low-weight unpolymerized radicals and monomers in the surroundings of the focal spot, which tend to diffuse toward the polymerized voxel causing it to grow in a more isotropic fashion. The first mechanism defines the voxel's aspect ratio on short time scales, while for prolonged exposure the second one dominates.<sup>[46,47]</sup> DeVoe et al. confirmed these observations for an acrylic-based resin. However, the group observed a different behavior in the epoxy-based SU-8 photoresist, where they found that the aspect ratio of the voxel remains constant for short exposures.<sup>[48]</sup> From these contrasting observations, it is clear that the voxel scaling mechanism strongly depends on the chemistry and viscosity of the resin, and a more complex model is needed.

The experimental evaluation of the voxel size can be a non-trivial task because of the aforementioned effects. One of the most employed protocols is the ascending scan method,<sup>[49]</sup> schematized in Figure 2D, for which several voxels are polymerized at increasing heights from the substrate, allowing for the subsequent measurement of  $d$  and  $l$  from, respectively, the truncated and the collapsed voxels, by Scanning Electron Microscope (SEM) micrographs. Another technique is the suspended bridge method,<sup>[48]</sup> where a thin line is polymerized between two large structures of polymerized resist and it is better suited to observe voxels with lateral dimension below 100 nm, because those structures have difficulty surviving the development in the ascending scan method.

Different approaches to increase the resolution have been developed: i) fine tailoring of the optical system and the writing

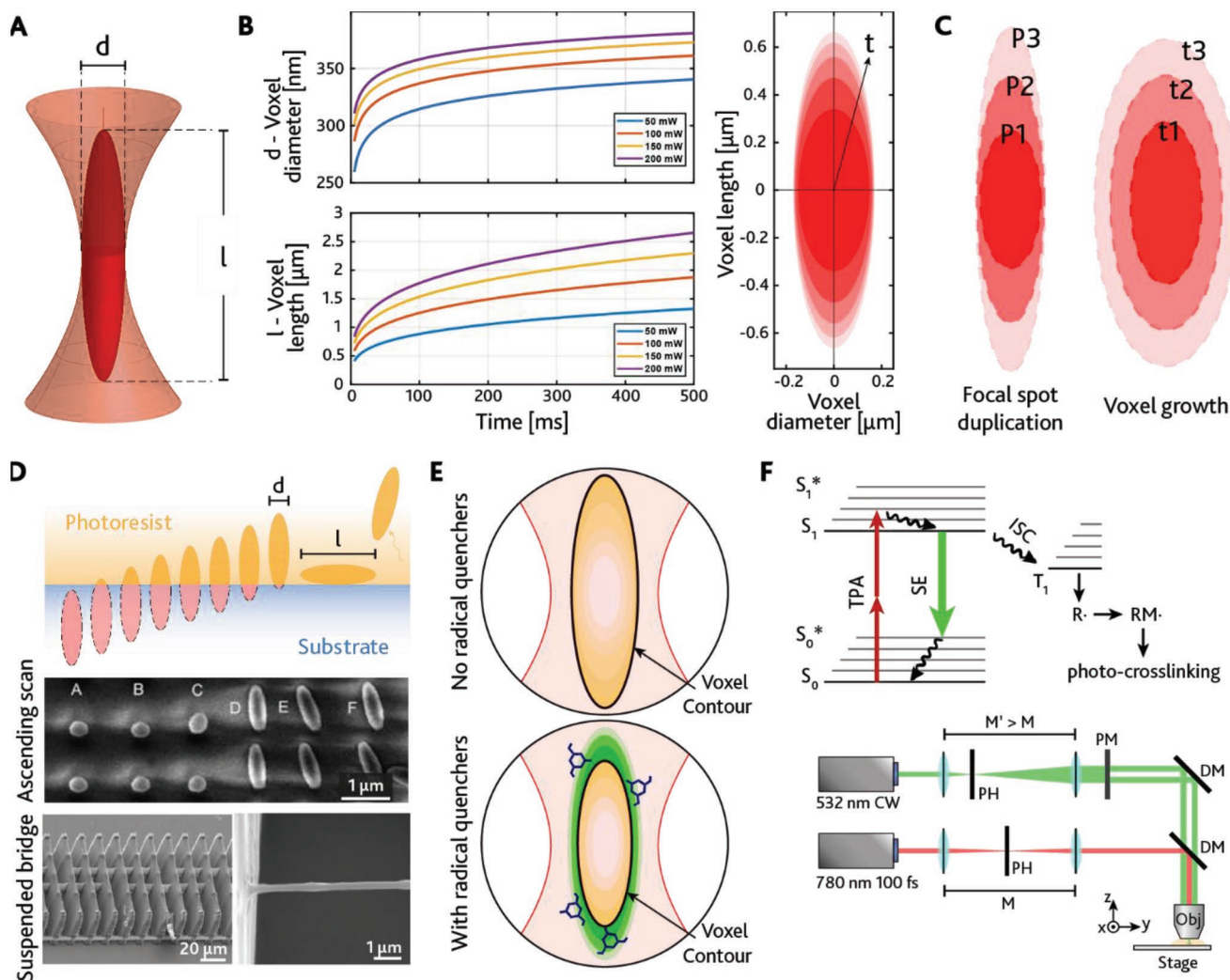


**Figure 2.** A) Representation of the polymerizing voxel in the focus of the laser beam, modeled as an ellipsoid with lateral dimension  $d$  and axial dimension  $l$ . B) (left) Numerical analysis of the scaling laws of the diameter (top) and length of the voxel (bottom) according to the linear-exposure model (Equations 3 and 4).  $\lambda = 780$  nm,  $NA = 1.4$ ,  $n_{oil} = 1.515$ ,  $\rho_0 = 0.024\%$ ,  $\rho_{th} = 0.0025\%$ ,  $\tau = 100$  fs,  $f = 80$  MHz,  $\delta = 3 \cdot 10^{-55}$  cm<sup>4</sup> s. (right) Size and shape of the voxel as a function of the exposure time  $t$ , extracted from plots on (left) for  $P = 50$  mW. C) Models for initial voxel formation and growth: focal spot duplication (left) and voxel growth (right). D) (top) Sketch and SEM micrograph of the ascending scan technique employed to measure voxel's diameter  $d$  and length  $l$ . SEM micrograph reproduced with permission.<sup>[49]</sup> Copyright 2002, AIP Publishing. (bottom) SEM micrographs for the suspended bridge method, employed to measure the resolution of the TPL system. Reproduced with permission.<sup>[48]</sup> Copyright 2003, Society of Photo-Optical Instrumentation Engineers (SPIE). E) Schematic representation of the voxel size without radical quenchers (top) and with added radical quenchers (bottom). The voxel contour is reduced when radical quenchers are added to the photosensitive resin. F) (top) Energy diagram of the depletion mechanism in a STED process. Excited molecules in the external region of the voxel are forced to stimulated emission (SE) and cannot undergo intersystem crossing (ISC) to initiate the polymerization process. (bottom) Optical setup employed for STED TPL. CW: continuous wave. PH: pinhole, PM: phase mask, DM: dichroic mirror, M: magnification, Obj: objective lens.

parameters, ii) adding radical quenchers in the photoresist, and iii) employing STED-like lithography techniques to partially deplete the focus region from radicals, thus reducing the size of the voxel. Regarding i), the properties of the objective lens play a key role in defining the resolution of the system. In TPP optical setups the laser beam is magnified with a beam expander to fill the back aperture of a high NA, high magnification objective. Indeed, the resolution scales laterally with  $NA^{-1}$  and axially with  $NA^{-2}$ , and for this reason, oil-immersion objective lenses with high  $NA \approx 1.4$  are largely used.<sup>[50]</sup> Together with that, the fabrication parameters, including average power, exposure time, and

optical dosage, heavily influence the voxel shape and size.<sup>[51,52]</sup> In TPP systems those parameters can be easily controlled and changed in real-time with additional equipment on the optical path, such as acousto-optic modulators (AOMs), Pockels cells, or polarizers for the average power, or electro-mechanical shutters in the case of the exposure time.

Concerning point ii), Equation 2 describes the principal mechanism behind the radical polymerization reaction, in which free radicals  $R^{\cdot}$  combine with monomers  $M$  to form longer polymeric chains.<sup>[53,54]</sup> This process can be hindered by adding radical quenchers ( $Q$ ) in the resin that can deactivate

the photo-induced radicals in the focal spot:  $R^{\cdot}$  combines with  $Q$  instead of  $M$ , terminating the chain reaction and partially preventing polymer's growth:<sup>[55]</sup>



The concentration of optically generated radicals is proportional to the square of the intensity, therefore, at the center of the focus the density of radicals is high enough to initiate the polymerization, while in the external region of the focal volume, the process is hindered by the presence of the quenchers, resulting in a reduction of the voxel volume, and an improvement in the resolution (Figure 2E). For instance, Takada et al.<sup>[56]</sup> improved the writing resolution from 120 to 100 nm when adding quenchers to the resin in a concentration of 0.8 wt%. It should be considered, however, that the quenching effect could reduce the mechanical qualities of the structures due to the shorter length of the chains.<sup>[57]</sup>

Regarding point iii), the voxel dimension can be further engineered by employing more sophisticated techniques that fall under the STED-like umbrella. STED is a technique that has been introduced in the field of fluorescence microscopy to increase resolution and contrast by reducing the fluorescence generated outside of the focal point.<sup>[58]</sup> In conventional TPP, PI molecules in the ground singlet state  $S_0$  are promoted to the excited singlet state  $S_1$  by TPA, then the excitation proceeds to the triplet state  $T_1$  via intersystem crossing (ISC) and generates a radical  $R^{\cdot}$  which initiates the chemical reaction.<sup>[59]</sup> The schematics of the setup with the Jablonski diagram of the STED process are reported in Figure 2F. By employing this technique, Wollhofen et al.<sup>[60]</sup> achieved a writing resolution of 55 nm, while Fischer et al.<sup>[61]</sup> demonstrated an improved accuracy in the fabrication of photonic crystals. In addition to STED lithography, several techniques based on different depletion mechanisms have been proposed. In Photo-Inhibited Super Resolution (PInSR) inhibition molecules are added to the resin and are used to generate radical traps by the deactivation beam, to react with the polymeric chain and terminate the reaction.<sup>[42,62]</sup> Li et al. proposed Resolution Augmentation through Photo-Induced Deactivation (RAPID) lithography,<sup>[41]</sup> in which a particular photo-initiator can be deactivated by the same wavelength of the excitation beam (800 nm), thus having the peculiar property that a higher optical dosage causes less polymerization.<sup>[63]</sup> With RAPID, the group achieved an axial resolution of 40 nm ( $\lambda/20$ ). Other techniques include Two-Color Photo-initiation/Inhibition,<sup>[64]</sup> or Resist Heating,<sup>[65]</sup> in which via a repeated process of absorption and non-radiative decay to vibrational levels of the same excited state, the resist is heated, and its mechanical properties can be changed by the effect of the temperature.

### 3. High Speed/High Throughput TPL

One of TPL main drawbacks compared to other lithography techniques is the relatively long writing time, which limits its utilization for mass-scale production. In the last decade, commercially available two-photon direct laser writing systems have emerged<sup>[66]</sup> (Nanoscribe, Multiphoton Optics, UP Nano, and

Femtika); these systems represent the state-of-the-art for general purpose TPL, being precise, versatile, and user-friendly, and they may also integrate specific equipment to perform laser ablation and welding. However, due to the high cost and relatively low throughput, their application is mostly limited to research purposes. Despite these novelties, performing machines, the vast majority of TPL systems in research labs consist of custom-made setups built around specific needs, with each setup being different in terms of laser, optical components, positioning systems, and photoresists.<sup>[54]</sup> This makes it difficult to define a quantitative benchmark for the writing speed. Indeed, the achievable fabrication speed depends on a multitude of parameters, such as optical dosage, scanning method, substrate motion system, chemical properties of the resist, and so on.<sup>[67]</sup> All these aspects need to be carefully optimized to consistently reduce the fabrication time. In this Section, we describe the most employed strategy reported in the literature to increase the speed and/or throughput of TPL.

#### 3.1. Optimizing Writing Speed and Fabrication Time

A well-known rule in the field of planar lithography and micro-fabrication is the Tennant's law (Equation 7), which links the resolution  $Res$  [nm] of the lithography system with the throughput  $TP$  [ $\text{nm}^2 \text{h}^{-1}$ ] of the process,<sup>[68]</sup> and is given by the power law:

$$TP_{2D} = C_{2D} Res^5 \quad (7)$$

where the subscript 2D refers to a planar fabrication, and  $C_{2D}$  is a constant which depends on the efficiency of the process. Tennant's law can be extended in a 3D fabrication process following the area-to-volume scaling:<sup>[69]</sup>

$$TP_{3D} = C_{3D} (Res^5)^{2/3} \quad (8)$$

which is better suited for estimating TPP throughput. In Equation 7, the fifth power law shows how a better (i.e., smaller) resolution strongly hinders the throughput of the process and conversely increasing the throughput by reducing the fabrication time should come at the expense of the resolution. An estimation of the fabrication time strictly related to TPL was proposed by Malinauskas et al.:<sup>[70]</sup>

$$t_F = \frac{xyzF}{Rv} \quad (9)$$

where  $t_F$  is the fabrication time,  $x$ ,  $y$ , and  $z$  are dimensions of the object in the three directions,  $F$  is the filling factor (ratio between the polymerized volume and the non-polymerized volume of the final object),  $R$  is the cross section of the voxel in the focal plane, and finally  $v$  is the writing speed. The parameter  $R$  depends on the size of the voxel, which in turn depends on  $NA$  and writing power, as described in Section 2.2. However, Equation 9 does not consider other factors such as the chemical properties of the resist and the time required for the repositioning of the beam and therefore gives only a qualitative estimation of the fabrication time.

Writing speed  $v$  refers to the speed at which the laser focus can be moved with respect to the substrate when defining the object geometry. The voxel movement can be attained by employing galvanometer-based optical scanners (galvoscan-

ners or galvo), multiple-axis linear translational stages, or more frequently, a combination of the two technologies<sup>[71]</sup> (Figure 3A). Galvoscan-

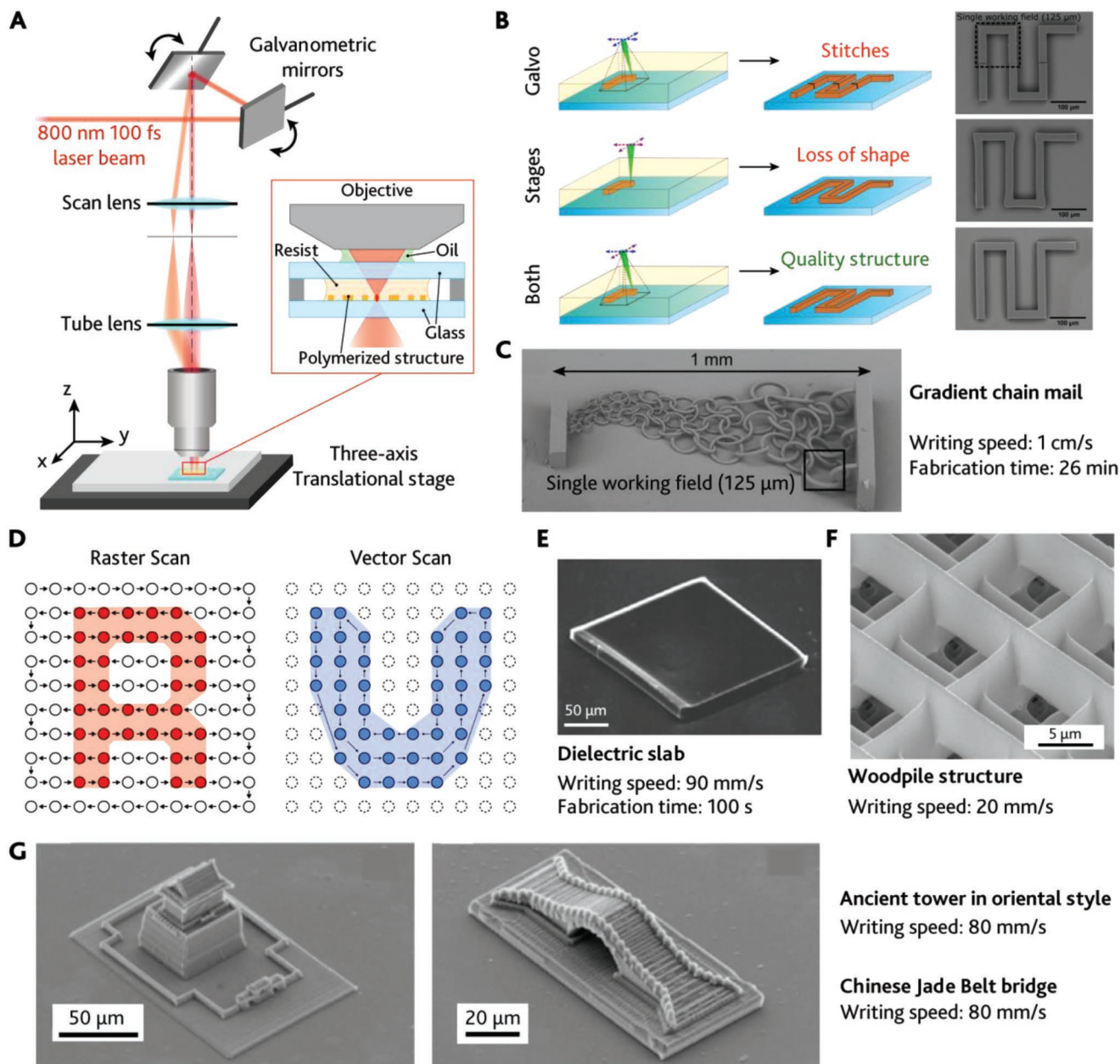


**Figure 3.** A) Typical setup for TPL beam. After the initial conditioning (not shown), the beam is coupled to a pair of galvanometric mirrors which scan the beam in the  $[x, y]$  plane. The reflected beam is directed in the high NA objective lens by a scan lens–tube lens pair, and it is focused on the sample. The substrate of the sample is mounted on a three-axis translational stage for positioning in all directions. B) Schematics of TPL using only galvoscan-

configuration, which can be quickly rotated around their axis, thus allowing the scan of the beam in two dimensions. The scanning beam is then relayed to the objective lens' back aperture allowing the scan in the objective Field Of View (FOV). Galvanometric actuators are very precise, with short latency time in the order of a few hundreds of microseconds, and therefore allow the rapid scanning of the mirrors in the kHz frequency domain with a good angular resolution. This results in a beam scanning speed that is in the order of  $\text{cm s}^{-1}$  (or even  $\text{m s}^{-1}$ ),<sup>[72]</sup> even if the actual writing speed may be limited by other factors. As an example, NanoScribe declares a maximum scan speed of  $625 \text{ mm s}^{-1}$  and a minimum feature size of  $160 \text{ nm}$  for their commercially available Photonic Professional GT2 system.<sup>[73]</sup> One of the main drawbacks of galvoscaners is that the scanning of the beam is limited inside the FOV of the microscope: since TPL employs objective lenses with high NA and magnification, this domain is usually limited to  $\approx 0.02 \text{ mm}^2$  ( $\approx 140 \times 140 \text{ }\mu\text{m}$ ). This limited range does not represent a problem when polymerizing small objects, however, larger patterns need to be realized by stitching together different fabrications made on smaller areas, potentially inducing structural errors during the stitching process.<sup>[74]</sup> Another limitation of galvoscaners arises when the structure dimension approaches the boundaries of the objective lens FOV, due to focusing aberrations.<sup>[75]</sup> Although TPL can be performed relying only upon galvoscaning without using any translation linear stage to move the sample in the  $[x, y]$  plane, a linear stage is required to move the sample along the Z-direction, in order to achieve real 3D fabrication.<sup>[76]</sup>

The second option to control the relative movement between the polymerization voxel and the sample consists in using translational stages to move the substrate along the three directions with respect to a fixed laser spot. Translational stages have the advantage of not being limited by the FOV's objective, with a travel range that can exceed tens of mm along each direction.<sup>[70]</sup> Conversely, translating stages are limited by a lower scanning speed with respect to galvoscaners (in the order of  $\text{mm s}^{-1}$ ), which is reflected on the total fabrication time. Moreover, since translational stages are much bulkier and heavier than galvo mirrors, the acceleration is reduced. For instance, motorized translational stages by Thorlabs reach a maximum speed of  $7 \text{ mm s}^{-1}$ , with a maximum acceleration of  $5 \text{ mm s}^{-2}$ , which is further reduced when additional components are installed on top of the stage, resulting in a non-uniform traversing speed along the travel range of the stage (galvoscaners are less affected by this issue due to the much lower inertia). This implies that some time is required before reaching the steady-state speed, thus resulting in imprecise timing with the shutter, which can lead to defective fabrications, in particular when polymerizing finer structures at high-speed. Air-bearing stages can reach a maximum speed of several hundred  $\text{mm s}^{-1}$  with an accuracy of  $100 \text{ nm}$  and are used to mitigate the disadvantages of translational stages; however, they are more expensive and require additional equipment.<sup>[54,77]</sup>

In general, the most versatile solution consists in employing both galvoscaners and translating stages: galvoscaners allow moving the beam in the FOV with high speed and accuracy, and translating stages are used to compensate for the reduced FOV of the objective. Several TPL systems also feature a second

set of three-axis translating stages: the first set consists of fast stages with a large travel range for a faster coarse positioning of the sample, while the second set employs slower and more precise piezoelectric stages for fine positioning, to move the substrate with nanometric precision over a travel range of a few hundreds of micrometers. To extend the FOV, some systems relying on galvoscaning employ a third galvo mirror to compensate for the loss of virtual conjugation between the main mirror pair, thus allowing fabrication of sub-micrometric features in a FOV of  $\approx 400 \times 400 \text{ }\mu\text{m}$  and limiting the need of pattern stitching.<sup>[78]</sup> Kumi et al. fabricated straight lines at a speed of  $1 \text{ cm s}^{-1}$  by extending the range of motion of the translation stage beyond the pattern size to allow for the acceleration time required to reach the steady-state speed.<sup>[79]</sup> Despite the impressive speed achieved, this method lacks the accuracy required for the fabrication of ordered periodic structures, since a temporal delay of a few milliseconds resulted in structures that varied in length by tens of micrometers (faster electronics could mitigate this issue). Another solution to compensate the low acceleration of translating stages proposes to modulate the laser power according to the instantaneous speed of the stage, namely reducing the power in the acceleration and deceleration segments to ensure a constant optical dosage.<sup>[71]</sup> Modern TPL systems aim at combining both the technologies for high-speed fabrication of complex structures. In a recent implementation, researchers fabricated 3D objects at a speed of  $10 \text{ mm s}^{-1}$  by synchronizing translation stages with galvoscaners to allow a continuous scan while simultaneously moving the working FOV to avoid both pattern stitching and loss of shape caused by stages acceleration<sup>[80]</sup> (Figure 3B,C). The task can be computationally demanding depending on the geometry of the structures, especially at high fabrication speeds, where a delay of microseconds can result in micrometric displacement that can compromise the quality of periodic structures like photonic crystals.

Independently from the method of choice employed to move the voxel with respect to the substrate, two basic scan modes can be distinguished: raster-scan mode,<sup>[59,81]</sup> and vector-scan mode,<sup>[59,82]</sup> schematized in Figure 3D. In raster mode, the focal spot must scan all the voxels in the cubic volume that encloses the target microstructure, independently from its final shape. For each slice of the micro-object, one axis is scanned rapidly, while the other moves slowly, and in each discrete position the shutter is open or closed depending on the desired geometry. In vector-scan, a 2D vector is traced in the writing plane by moving the mirrors or the stages, to directly trace the pattern to be defined. While raster-scan is more straightforward to implement, vector-scan requires a more refined algorithm and a closed loop feedback to control the mirrors. Typically, vector-scan requires less voxels than raster-scan and in some applications can reduce the fabrication time by 90% depending on the geometry of the micro-object.<sup>[59]</sup> Raster-scan remains the method of choice when producing structures with complicated shapes, high filling-factor, or that require a high accuracy.

As discussed in Section 2.1, negative TPP employs a laser beam to start a localized chemical reaction inside a very small volume, to make a material insoluble in the exposed region.<sup>[5]</sup> In the extensive literature of TPL a multitude of reactions is demonstrated,<sup>[83]</sup> spanning from the common radical polymerization of acrylates,<sup>[84–86]</sup> cationic polymerization of epoxies,<sup>[87,88]</sup> as



well as silicones<sup>[89,90]</sup> and ceramics.<sup>[91,92]</sup> Each of these materials has its own viscosity,<sup>[93]</sup> optical properties,<sup>[94]</sup> and kinetics,<sup>[95]</sup> and for this reason the writing time is also strictly related to the material being processed and does not depend only on the scanning speed of the laser spot, thus making it difficult to generalize about fabrication speed. For a given material, the polymerization reaction depends also on the peak power of the beam, pulse duration, and repetition rate. All these parameters can range in orders of magnitude, giving rise to several secondary effects that can hinder or promote the polymerization reaction, affecting the duration and quality of the process. A desirable quality for a good resin is a high dynamic range,<sup>[71]</sup> which can be defined as the ratio of damage threshold power to the polymerization threshold power at a given scanning speed. Since the acceleration is not constant, the resin will experience different optical dosages until a constant speed is reached: a resin with poor dynamic range could boil at the end point of the writing, where the speed is lower and exposure time is higher, or conversely be underexposed in the constant speed range, resulting in weaker cross-linking. A resin with good dynamic range can be used to write at a higher speed since it can sustain the increased power required to keep optical dosage constant. Under these high-power, high-speed conditions, a high dynamic range ensures that the resin is resilient to fluctuations or rapid variations of power and traversing speed without incurring in resist damages or explosions. Custom-made photo-initiators with high dynamic range and large TPA cross sections have proven to increase the speed of the polymerization.<sup>[96–98]</sup> Perry et al.<sup>[99]</sup> synthesized a resin with a dynamic range of 50 and a TPA cross section of 900 GM (1 GM =  $10^{-50}$  cm<sup>4</sup> s molecules<sup>-1</sup> photons<sup>-1</sup>) which allowed polymerizing a slab structure with a speed of 90 mm s<sup>-1</sup>, reported in Figure 3E. In a more recent work,<sup>[37]</sup> researchers achieved lower polymerization thresholds by developing custom initiators with high TPA cross section, or resins with modest dynamic range but with a low fluorescence quantum yield, more likely to generate radicals than to emit radiatively, which allowed fabricating real 3D objects with a speed of 80 mm s<sup>-1</sup> (Figure 3G). Indeed, the choice of the photo-initiator should be tailored according to the material which is being processed. As an example, since most commercial photo-initiators have limited initiating efficiency in aqueous solutions, Zheng et al.<sup>[100]</sup> proposed a non-toxic and water-soluble photo-initiator based on carbazole derivatives and cucurbit[7]uril. The host-guest interaction between the compounds has been shown to increase the TPA cross section from 613 to 2999 GM, while also improving the water solubility, opening to the fabrication of biocompatible 3D hydrogel scaffold for living cell culture.<sup>[101]</sup>

Also the temperature and heat accumulation plays a key role in determining the maximum speed at which the voxel can be scanned on the substrate.<sup>[102]</sup> The thermal diffusion time of the photopolymers at the focal point is in the order of  $\approx 15$   $\mu$ s,<sup>[71]</sup> if the time between two consecutive laser pulses is shorter than this time (repetition rate > 70 kHz), heat cannot dissipate properly, locally increasing the temperature of the resin. Higher temperature promotes the polymerization process, resulting in thicker lines and worse resolution. Baldacchini et al.<sup>[103]</sup> experimentally verified this thermal accumulation effect by chopping the pulses of a 100 fs 80 MHz laser with an AOM to deliver

to the sample 1  $\mu$ s bursts with varying dwell times between the bursts. Even when keeping the net fluence constant, the researchers observed smaller lines when the time between the bursts was larger. The Juodkakis group further confirmed these results;<sup>[104]</sup> moreover, in another work<sup>[105]</sup> the same authors proposed that for very high intensities, in the order of TW cm<sup>-2</sup>, the polymerization reaction is dominated by avalanche ionization rather than TPA. Avalanche ionization<sup>[105,106]</sup> is a process in which an unbound electron is accelerated by the electric field of the laser beam, and by interacting with other bonding electrons provides them enough energy to excite them to an unbound state, in a self-repeating process. Since accelerated electrons can propagate outside of the focal volume, once radicals have been generated by TPA, many more will be generated by avalanche ionization, promoting polymerization outside of the voxel and causing bigger linewidth. Those effects may be mitigated by reducing the repetition rate and the energy per pulse of the laser beam; however, this will come at the expense of the writing speed. Indeed, if thermal accumulation has to be minimized to achieve the best resolution, LaFratta<sup>[71]</sup> defined the “thermal limit” of the fabrication speed to be 10 mm s<sup>-1</sup>: the repetition rate for 15  $\mu$ s time intervals would cause adjacent voxels to be spaced  $\approx 150$  nm, which is a suitable distance for creating 3D objects, while for higher writing speed would cause the voxels to not overlap, a condition incompatible for the realization of 3D structures. These thermal effects need to be considered when the priority is the writing resolution, but for most applications of TPL, repetition rates in the order of MHz are perfectly acceptable. Nevertheless, these and other studies<sup>[107,108]</sup> proved that the mechanisms behind TPP are not limited to TPA, but also other effects may play an important role.

### 3.2. High-Throughput Non-Holographic TPL Techniques

Conventional TPP microfabrication is a serial process, in which microstructures are created on a voxel-by-voxel basis. Over the years, different methods to surpass this paradigm have been proposed, striving at parallelization and mass production of TPP-based microstructures. These can be non-holographic and holographic solutions, with these latter exploiting Spatial Light Modulators (SLMs) and/or Digital Micromirror Devices (DMDs) to dynamically structure the wavefront of the light impinging on the sample to expose the resist in a 3D fashion. While holographic methods are discussed in the next section, this one focuses on static solutions (i.e., methods which do not require a dynamically addressed modulation device to achieve 3D multi-beam patterning). Non-holographic methods are mostly based on i) micro-lenses arrays placed on an optical plane conjugated with the focal plane to perform multi-beam writing, ii) modulation of the beam intensity through optical masks, iii) interference lithography and phase masks, or iv) physical replication of an initial master structure to achieve mass-scale production.

#### 3.2.1. Micro-Lenses Arrays

Micro-Lenses Arrays (MLAs, sketched in Figure 4A) are optical elements composed of many small lenses on a

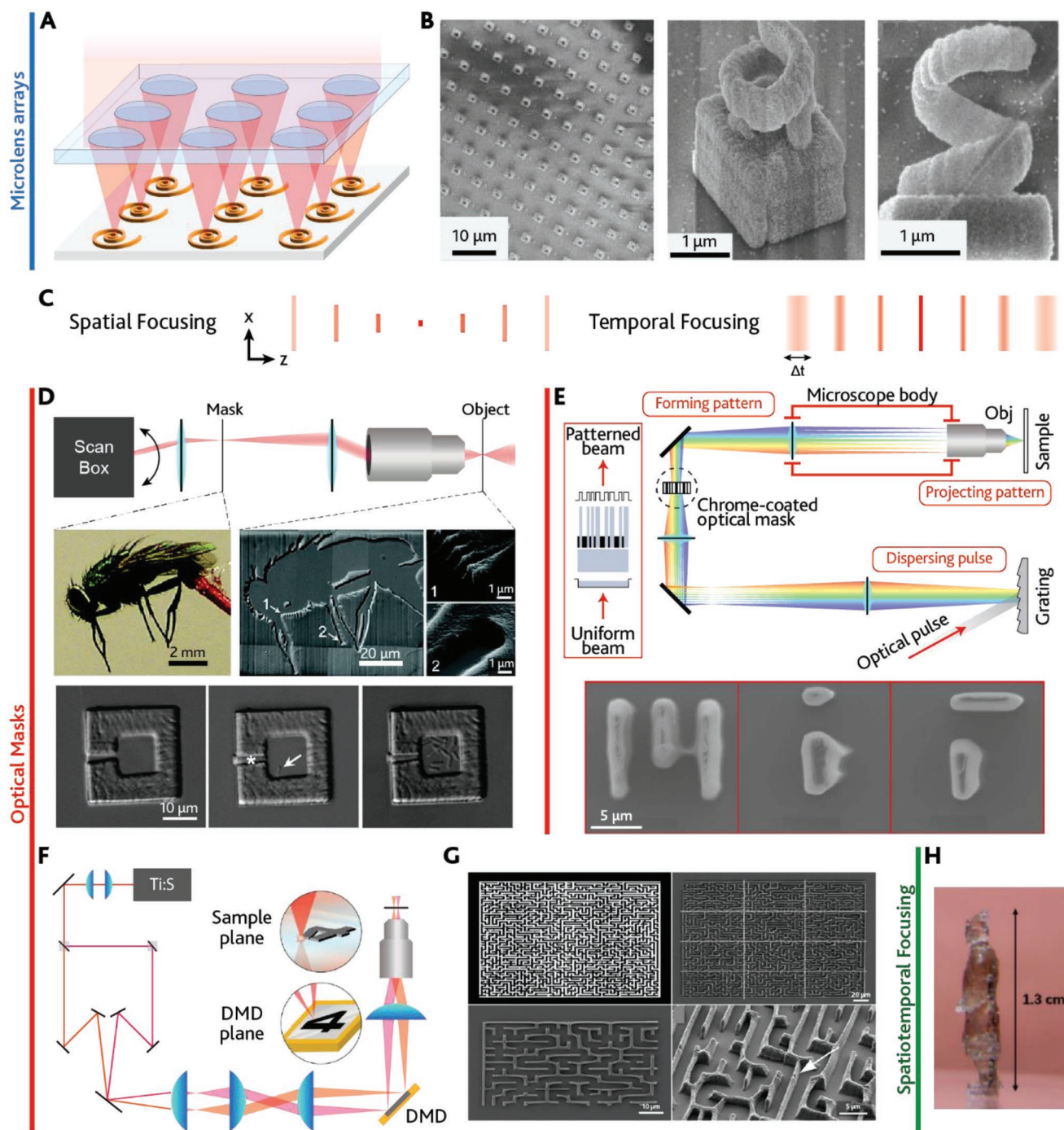


**Figure 4.** A) Schematic representation showing how a microlens array can generate multiple foci from a single laser beam. B) SEM micrographs of an array of micro-coils fabricated with MLA-based TPL. Reproduced with permission.<sup>[110]</sup> Copyright 2006, Optical Society of America. C) Sketch schematizing the difference between spatial focusing (left) and temporal focusing (right). In temporal focusing the beam covers an area many orders of magnitude larger than a diffraction-limited spot. High peak intensity at the focus is achieved by modifying the temporal profile of the pulse. D) Mask-directed TPL. (top) The object mask is placed in a plane conjugate of the objective focal plane, to fabricate a negative of the object. (bottom) Fabrication of a microtrap for a single bacterium. Adapted with permission.<sup>[118]</sup> Copyright 2007, American Chemical Society. E) (top) Schematic of a TPL system exploiting optical masks and temporal focusing. (bottom) 3D microfabrication of MIT logo. Adapted with permission.<sup>[119]</sup> Copyright 2010, Optical Society of America. F) Optical setup for TPL employing a DMD as an optical mask. The beam is split in two sub-beams to sample different regions of the DMD simultaneously. G) Protein-based maze fabricated using two independent scanning foci, with the setup shown in (F). Panels F and G adapted with permission.<sup>[120]</sup> Copyright 2012, Royal Society of Chemistry. H) Terra Cotta warrior taller than a centimeter, fabricated exploiting SSTF TPL. Reproduced with permission.<sup>[121]</sup> Copyright 2018, Wiley-VCH GmbH.

transparent substrate, where the size of each lens is in the order of hundreds of micrometers. A relatively small MLA can contain hundreds of lenses on its active surface. In MLA-based TPP, the collimated femtosecond-pulsed beam passes through the MLA and is then relayed in the objective lens, generating hundreds of spots on the writing plane. By moving the substrate with translating stages, it is possible to fabricate a large number of identical structures in parallel, decreasing the fabrication time of a factor equal to the number of the lenses in the array. An early example was reported in a work by Formanek et al.,<sup>[110,111]</sup> in which a  $50 \times 50$  square MLA of 300  $\mu\text{m}$ -diameter lenses was used to fabricate a large-area lattice of micro-springs, then a subsequent step of electroless plating of silver<sup>[112]</sup> allowed for the realization of complex metallic structures, reported in Figure 4B. The same group also reported the realization of large-area arrays of micro-letters and other micro-objects.<sup>[113]</sup> A crucial and challenging aspect of MLAs is that the beam intensity should: i) be homogeneous before passing the MLA, to avoid non-uniform structures between the extremities and the center of the FOV, ii) be high enough to allow each beamlet to exceed the polymerization threshold. Despite being well suited for the fabrication of arrays containing replica of the structure with a constant period, this approach is not ideal for fabricating arbitrary patterns of large FOVs. Because of those drawbacks and the advent of holographic methods applied to lithography, MLA-based TPL no longer finds widespread use; conversely, TPL has become one of the most employed techniques for the fabrication of MLAs for generic purposes.<sup>[114–117]</sup>

### 3.2.2. Transparency Masking

A different approach consists in using optical/transparency masks placed in a conjugated plane of the focus to create a point-to-point mapping within the writing plane. The basic concepts rely on raster scanning the laser beam on a mask which transposes any intensity modulation of the mask plane on the writing plane, projecting a negative replica of the image on the mask into the photoresist. Kaehr and Shear used a house fly as a mask to first demonstrate this approach, then used the same method for direct photo-crosslinking of proteins to fabricate microchambers for the trapping of bacteria<sup>[118]</sup> (Figure 4D). Kim et al. adapted this concept demonstrating wide-field layer-by-layer fabrication of 3D structures using a chrome-coated optical mask.<sup>[119]</sup> In the work, the authors achieved wide field by temporally dispersing femtosecond laser pulses with a reflective dispersion grating, and by temporally re-focusing them on the writing plane, as reported in Figure 4E.

The main advantage is that there is no need to raster-scan the mask, and the fabrication speed is not dependent on the size of the features on the mask. A downside is that this temporal-focusing approach<sup>[122]</sup> requires higher peak power compared to more conventional raster-scanned spatial-focusing. The main limitations of mask-based TPP are the time required to fabricate the optical masks, and the need for their precise positioning on the optical path, as a shift of a few millimeters along the optical axis, can greatly degrade the resolution.

Nielson and coworkers used a DMD to define digital masks, avoiding the fabrication of the mask and limiting alignment issues. The active surface of the DMD was raster scanned, and the beam was reflected inside the objective lens depending on the state of each micro-mirror to create patterns at the impressive speed of  $3 \text{ cm s}^{-1}$ .<sup>[123]</sup> This method was further improved: by splitting the beam into two sub-beams it was possible to sample different regions of the DMD simultaneously to fabricate non-periodic structure in a large area in a half the time<sup>[120]</sup> (Figure 4F,G). Moreover, by partially overlapping the scan area of the two beams it was possible to create crosslinking-density gradients at the microscale. Concerning DMD-based TPL, recently Liu and coworkers demonstrated MaskLess Optical Projection NanoLithography (MLOP-NL), a technique capable of patterning nanometric features over a large-area spanning hundreds of micrometers.<sup>[124]</sup> The authors exploited a femtosecond pulsed laser with a central wavelength of 400 nm and a DMD to expose the AR-N 7520 negative photoresist with a predetermined pattern, achieving a minimum feature size of 32 nm ( $\lambda/12$ ) when addressing a single pixel of the DMD. MLOP-NL was employed to design batch patterns such as bidimensional structures with nanometric gaps<sup>[125]</sup> or FinFETs (Fin Field Effect Transistors) on a large scale, as well as arbitrary photolithography masks,<sup>[124]</sup> paving the way for applications in microelectronics and biotechnological micro- and nano-devices.

More recently, Saha et al. exploited a DMD and simultaneous spatiotemporal focusing (SSTF), achieving parallel fabrication without undermining the writing resolution.<sup>[126]</sup> This allowed writing a  $2 \times 2 \times 0.25 \text{ mm}$  cuboid in 8 min rather than a few hours. SSTF was also exploited to fabricate 3D objects taller than a centimeter<sup>[121]</sup> (Figure 4H).

### 3.2.3. Interferometric TPL

Techniques based on interference lithography<sup>[127–129]</sup> (IL) offer an alternative for the realization of complex 3D structures. Those methods can be implemented with SPA, however, the use of TPA allows to further improve the resolution. The first demonstration of multi-beam IL was proposed in 1999 by Kirkpatrick and coworkers: two 800 nm fs-pulsed beams impinge the sample from different directions, creating a 3D complex pattern to expose the photoresist on a large area. In their work, the authors realized a  $1 \text{ mm}^2$  2D periodic grating by exposing the photoresist for  $\approx 5 \text{ min}$ .<sup>[130,131]</sup> In the method presented by Kondo et al., reported in Figure 5A, the beam was split with a diffractive beam splitter, and the beamlets were refocused on the writing plane with a pair of lenses to ensure the temporal overlap of femtosecond pulses.<sup>[132]</sup> The desired interference pattern is achieved by placing an aperture array in the Fourier plane between the lenses to select only a subset of the generated beamlets. By exposing a layer of SU-8 photoresist with 800 nm pulses of a Ti: Sapphire oscillator with four beamlets, the group was able to fabricate structures with a 2D periodicity on the writing plane, and homogeneous along the axial direction, since the axial components of the wave-vector of the four beams were the same (Figure 5B). More recently, Maibohm et al. proposed a fixed diffractive optical element (DOE) to split

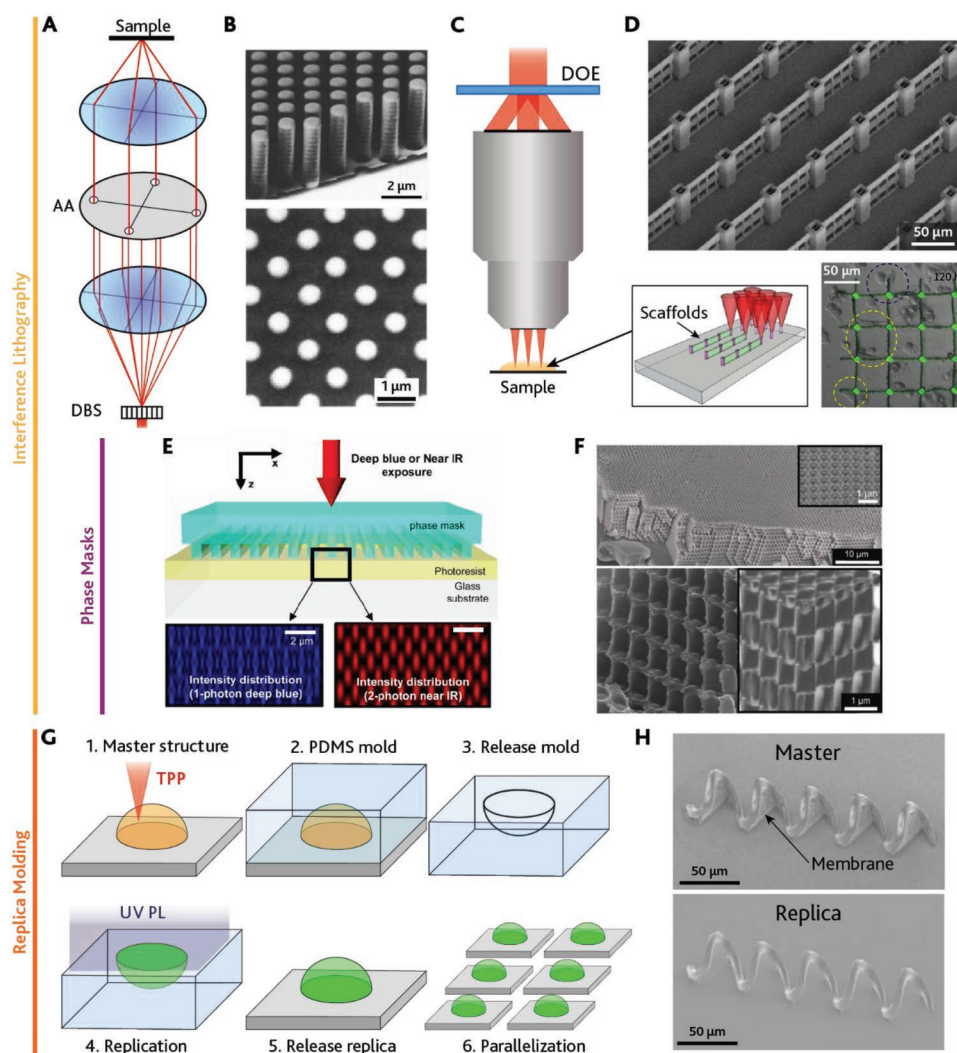


**Figure 5.** A) Optical setup for IL proposed in Ref. [132] DBS: diffractive beam splitter, AA: aperture array. B) SEM micrographs of the structure fabricated by the four-beam interference. (top) Oblique view, (bottom) top view. Adapted with permission.<sup>[132]</sup> Copyright 2003, AIP Publishing. C) Representation of the TPL setup in Ref. [133] The beam, passing through the DOE is split in 9 beamlets (shown in inset). D) Result of the fabrication of scaffolds for cell growth. The inset shows cells incubated on the microstructures. Reproduced with permission.<sup>[133]</sup> under terms of the CC-BY license. Copyright 2020, The Authors, published by Springer Nature. E) Schematic illustration of a phase mask working, showing the intensity distributions generated by 405 and 810 nm exposure. F) SEM images of 3D structures made with TPL with a phase mask. (top) Large area angled view and top view, (bottom) cross sectional views at different angles. Panels E and F adapted with permission.<sup>[136]</sup> Copyright 2006, Optical Society of America. G) Schematic of the  $\mu$ TM process, from a master structure made by TPL, molding in PDMS, and casting of replicas from the mold. H) SEM of a master structure for MA- $\mu$ TM (top) and resulting replica (bottom). MA- $\mu$ TM allows replicating structures with closed loops like the coil in figure. Reproduced with permission.<sup>[143]</sup> Copyright 2006, National Academy of Sciences, U.S.A.

the beam into multi-beamlet for parallelized writing on a large area.<sup>[133]</sup> The DOE creates a  $3 \times 3$  pattern of beams with a  $50 \mu\text{m}$  pitch to reduce the fabrication process by 9 times, as sketched in Figure 5C. With this iteration of IL, the group was able to fabricate  $450 \times 450 \mu\text{m}$  continuous arrays for cell scaffolds in less than an hour (Figure 5D).

Some implementations of multiphoton IL rely on phase masks<sup>[134,135]</sup> to take advantage of the periodic nature of light to expose the photoresist in a controlled fashion. Rogers and coworkers extended the field of IL by proposing proximity-field nanopatterning<sup>[136,137]</sup> (PnP), in which a 2D relief pattern is realized on the surface of polydimethylsiloxane (PDMS) elastomer.

This replica is pressed on a substrate covered with SU-8 photoresist to act as a phase mask, generating a complex 3D interference pattern to expose the resin (Figure 5E). PnP allowed fabricating woodpiles and 3D structures (Figure 5F) with sub-micrometric resolution over an area of  $0.25 \text{ mm}^2$  in a few minutes. An advantage on PnP over conventional multiphoton IL is that the phase mask can cover a surface as large as a silicon wafer, and the relief pattern can vary along its surface. This makes PnP a suitable technique for fabricating periodic or quasi-periodic patterns on a local scale, but also open the possibility to fabricate structures that can vary considerably over larger distances scale, given the possible non-uniformity of the phase mask.<sup>[44]</sup>

### 3.2.4. Master-Based Replica of TPL Structures

Some other parallelization techniques do not rely on structuring physical properties of the impinging beams but exploit post-processing solutions. One approach, usually referred as outer-shell fabrication,<sup>[138]</sup> consists in employing TPP only to define the external layer of a bulk 3D structure, then to solidify the internal volume of the object with a single-photon exposure process with a UV lamp. As an example, Sun and Kawata produced a 3D micro-bull by vector-scanning only 5% of the voxel required to define the entire volume in raster-scanning, then solidified the structure under a mercury lamp.<sup>[59,139]</sup> Albeit this required an additional SPA step, the TPP structure was fabricated in 13 minutes instead of the three hours required with raster-scan. Another approach that could increase the throughput of TPL is a soft lithographic replication technique known as Micro-Transfer Molding<sup>[140,141]</sup> ( $\mu$ TM). In  $\mu$ TM, an initial master structure or pattern is fabricated via TPP, then flexible PDMS is used to replicate elastomeric transfer molds of the master. Subsequently, the PDMS molds are filled with photoresist, which is photo-crosslinked with SPA exposure, to obtain several replicas of the original structure. A schematized representation of the process is reported in Figure 5G. In principle, the single TPP master structure can be employed to replicate tens of PDMS molds, and from each mold, one can expect a dozen of replicas before the material deformation. PDMS is the material of choice for the realization of the mold, as it is inexpensive, has good thermal stability, transparency, chemical resistance, and low Young modulus, which make it easy to separate the mold from the master or replicas.<sup>[142]</sup> This technique was used to replicate a large class of structures, including more complex geometries with overhangs, undercuts, and high aspect ratio; however, structures with holes or closed-loop encounter topological limitations and may be impossible to replicate with conventional  $\mu$ TM. LaFratta et al. proposed a solution to this problem with membrane-assisted  $\mu$ TM (MA- $\mu$ TM), in which a thin membrane is created inside each closed-loop during the master fabrication via TPP.<sup>[143]</sup> In the molding step the membrane prevents the PDMS to form a complete closed-loop, then the PDMS mold can still be removed from the master due to its elasticity. As an example, the authors reported the fabrication of a coil whose master structure had a membrane in each turn, to allow replicas with closed loops (Figure 5H). In MA- $\mu$ TM, the master structure can be fabricated with a high resolution with TPP, and the replicas can be reproduced in the same amount of time, independently on the finesse of the original master, in fact the PDMS mold can host several master structures that may take hours to fabricate, but when the mold is completed, it can replicate many copies of the master in a few minutes. Moreover, the replicas can be recreated with a material different than the original photoresist, since a wide range of materials can be cast in molds.<sup>[144,145]</sup> The main disadvantage of this approach consists of its topological limitation: even MA- $\mu$ TM cannot replicate porous structures with several closed loops, like photonic crystals, Cartesian 3D lattices, or scaffolds for cellular growth.

This section covered some of the strategies exploited in the field of TPL to increase the fabrication speed or to scale

the throughput of devices. Each of these techniques has its own intrinsic advantages and disadvantages, which can range from increased complexity of the optical system as in IL, the requirement of higher power of temporal-focusing as in MLA-based TPL, or the additional steps needed in  $\mu$ TM. It must be pointed out that these approaches, albeit very different, are not mutually exclusive: indeed, the fabrication of a single structure can be parallelized with IL or using MLAs to define a large area master, which could be quickly reproduced in a large number with  $\mu$ TM. However, these techniques cannot be employed to fabricate arbitrary geometries:  $\mu$ TM is limited by the topology of the master structure, MLAs can reproduce only several copies of the same object, and IL is limited to periodic patterns which can be repeated on a larger scale. Although the technologies reviewed in this section are clear examples of brilliant strategies for increasing TPL throughput, they have some limitations, mainly related to their static mode of operation. Alongside these technologies, in the next section lithography approaches relying on holography are discussed. Those techniques can reproduce arbitrary geometries both in 2D and in 3D by dynamically changing the phase of the beam wavefront to speed up layer-by-layer fabrication, or to generate multiple dynamically controlled foci in the writing plane to parallelize the writing process.

## 4. Holographic Two-Photon Direct Laser Writing

Fabrication over large areas, characterized by parallel replication of microstructures with high accuracy and high speed, received a leap forward with the technological development of Digital Micromirror Devices (DMD) or Spatial Light Modulators (SLM). The adoption of these devices, and in particular their integration in TPL optical setups, allowed to introduce holography principles in the framework of micro- and nanofabrication. This paved the way for a series of applications with unprecedented efficiency, including parallel writing of multiple features (multifoci generation) or dynamic phase shaping to control the beam focus properties. This in turn determined an improvement in the throughput and parallelization of TPL processes, which became a step closer to being considered as a viable mass-production technique.

A small clarification is due with respect to a possible lexical ambiguity: the expression Holographic Lithography is often considered a synonym for Interference Lithography, an approach, described in Section 3.2.3, whereby two or more beams are made to interfere, exploiting complex interference patterns focused on the writing plane to polymerize periodic structures. In the following, instead, holographic two-photon lithography (HoloTPL) is intended as the process to reconstruct a pre-determined wavefront within the photoresist to provide advanced control of the fabrication process. Next paragraphs will first describe the basic principles of holography and its integration with TPL which relies on Computer Generated Holograms (CGH). Then we will focus on two distinct implementations of HoloTPL: multifoci generation and focused beam shaping, this latter both in terms of proper 3D structuring and strategies to mitigate optical aberrations.

#### 4.1. General Aspects and Theoretical Overview

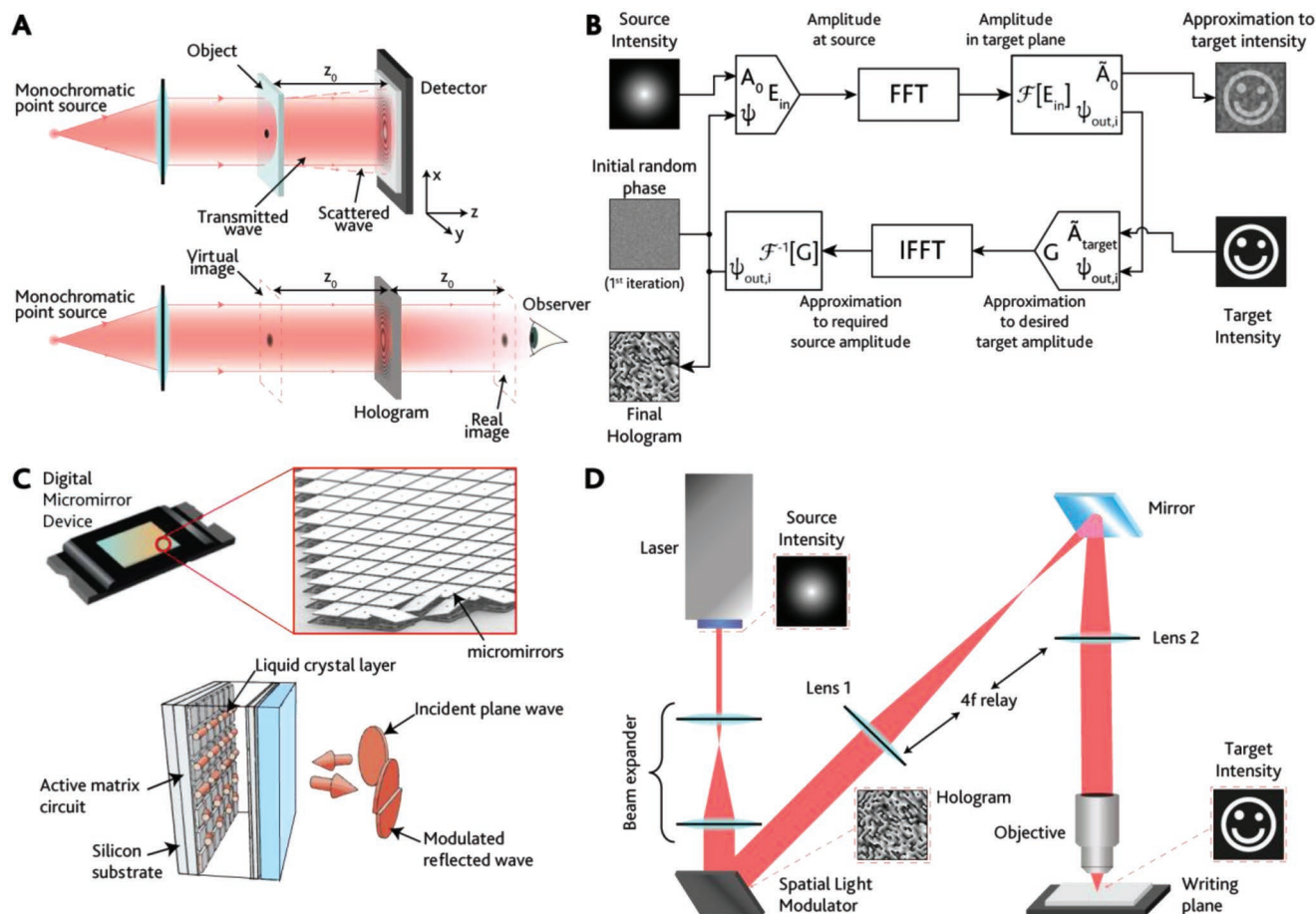
Holography was introduced by Gabor<sup>[146]</sup> in 1948, for which he was awarded the Nobel Prize in 1971. It refers to the possibility to record not only the intensity distribution of light diffracted by an object but also to retrieve the phase distribution of the scattered light, thus recording the complete wave field. This is obtained through the interference between the light scattered by the object upon illumination from a coherent monochromatic source (the object wave) and a reference plane wave (or spherical wave) from the same source. The interference between the object and reference wave will result in a pattern, called “hologram”, that shows no resemblance with the real object but that encodes both the amplitude and phase of the object wave, which can be recorded and reproduced, for instance, on the active area of a modulation device. The power of this strategy relies on the possibility to regenerate the object by illuminating the hologram with the reference wave. This property determined an outstanding interest from the scientific community spanning biotechnology,<sup>[147]</sup> neuroscience,<sup>[148,149]</sup> fiber-optics

technology,<sup>[150]</sup> metasurfaces,<sup>[151,152]</sup> and data storage,<sup>[153]</sup> just to mention a few.

##### 4.1.1. Wavefront Retrieval Methods

Many wavefront reconstruction methods have been proposed, modified, and optimized in the last decades,<sup>[154]</sup> with the most relevant for this work being the in-line Gabor hologram, the off-axis Leith-Upatnieks hologram,<sup>[155–157]</sup> and the Fourier holograms.<sup>[158–160]</sup> To outline the general idea behind wavefront reconstruction a simplified theoretical description of the in-line holograms will be given, thanks to the easiness of the method.

With reference to the simplified optical arrangement in **Figure 6A**, the object is illuminated by a coherent monochromatic source along an axis normal to the detection plate. The light arriving on the detector is composed of two terms, the first one being the directly transmitted light (reference wave), treated as a uniform amplitude and phase distribution over the detector area, with constant complex amplitude that can be



written as a real constant  $r$ . The second one is instead the scattered wave caused by the object, with complex amplitude  $o(x,y)$  with  $|o(x,y)| \ll r$ . The intensity on the detector plane is obtained by the sum of the complex amplitudes:

$$I(x,y) = |r + o(x,y)|^2 = r^2 + |o(x,y)|^2 + ro(x,y) + ro^*(x,y) \quad (10)$$

with  $o^*(x,y)$  being the complex conjugate of  $o(x,y)$ . Let the recorded transmittance be a linear function of the intensity  $I$ , for simplicity, of the type:

$$t = t_0 + \beta TI \quad (11)$$

with  $t_0$  a constant background transmittance,  $T$  the exposure time,  $\beta$  a parameter related to the detector characteristics. From Equation 10 the hologram can be obtained as:

$$t(x,y) = t_0 + \beta T [r^2 + |o(x,y)|^2 + ro(x,y) + ro^*(x,y)] \quad (12)$$

If this hologram is replaced in the same position as the detector, illuminating it with the same monochromatic beam used for the original recording with complex amplitude  $r$ , it is indeed possible to reconstruct the original  $o(x,y)$ . At any point, the complex amplitude of the beam after the hologram will be:

$$u(x,y) = rt(x,y) = r(t_0 + \beta Tr^2) + \beta Tr |o(x,y)|^2 + \beta Tr^2 o(x,y) + \beta Tr^2 o^*(x,y) \quad (13)$$

The first term is an attenuated plane wave (the transmitted beam), the second term can be neglected since  $|o(x,y)| \ll r$ , the third term  $\beta Tr^2 o(x,y) = \text{const} \cdot o(x,y)$  is identical to the original  $o(x,y)$  multiplied by a constant factor and it reconstructs an image in the same place where the original object was, while the fourth term resembles the original one but with an opposite curvature, and it forms a real image (the conjugate image) at the same distance from the hologram. This reconstruction approach implies many drawbacks: first, the in-line observer will simultaneously observe the reconstructed image, the out-of-focus conjugated image, and a strong background from the source; second, the object needs to have a high transmittance to neglect the second term in Equation 13. Nevertheless, this simplified description allows to introduce the basic idea underlying holography.

Other wavefront retrieval approaches have been introduced shortly after to address the drawbacks of the in-line method. Leith and Upatnieks<sup>[154,155]</sup> introduced the off-axis method, which separated the image and the conjugated one by using a separate reference beam obtained from the same source, incident on the detector with a certain offset angle. For offset angles large enough, the transmitted beam, and the real and the virtual images that form after hologram illumination are not overlapped. The possibility to separate the three contributions acquires particular relevance in the context of this review, thanks to the adaptation of these principles also to reflection applications and the isolation of just the image contribution on the focal plane. Another interesting wavefront retrieval strategy is represented by the Fourier holograms by Vander Lugt,<sup>[154,160]</sup> in which the Fourier transform of the complex amplitudes of the original and reference waves interfere. This method,

suitable for objects that lies on a single plane or with reduced thickness, can reconstruct the image by conjugating the hologram with the back focal plane of the objective lens. Fourier holograms have the property that the reconstructed image does not shift for translation of the hologram in its plane. Fourier holograms are the concept behind CGHs, discussed in the next section, and are regarded as the wavefront retrieval method that plays the most important role in lithography applications.

#### 4.1.2. Computer-Generated Holograms

It was almost twenty years after Gabor's work that one of the milestones for the use of holography in lithography was laid by Brown and Lohmann in 1966, with the first examples of CGHs.<sup>[161]</sup> CGHs benefit from the outstanding property by which the object for which a hologram is going to be generated does not even need to exist. Historically CGHs were introduced in the context of spatial filtering of signals (see ref. [162] for a historical review of CGH), and then they had important applications in other fields, including TPL by virtue of the freedom given to the user to polymerize arbitrary geometries.

The term CGH encapsulates a number of mathematical techniques for the digital generation of holograms, which can consequently be reproduced on a modulation device. The mathematical tool behind CGHs is the Fourier transform, in both one and two dimensions, and its numerical implementation, which is referred to by Fast Fourier Transform (FFT) algorithms. For a formally rigorous mathematical discussion of the discrete Fourier transform and FFT, see Ref. [163] CGHs can be classified on the basis of FFT discretization into point-oriented and cell-oriented ones. In the first category, each pixel is considered substructure-free and uniform, and each point in the computed hologram is transformed into the value of a single pixel. In the second class, on the contrary, the structure of each pixel may not be uniform and in some way may control the phase and amplitude. Modern algorithms, designed to optimize the computational load for CGH generation, are generally referred to by the term Iterative Fourier Transform Algorithm (IFTA) and aim to reduce the difference between the target intensity distribution and the one generated on the focal plane as a result of reflection on the hologram. IFTAs were initially proposed by Gerchbert and Saxton<sup>[164]</sup> (GS). The iterative procedure provided in IFTAs aims to convert a certain intensity distribution received as input  $I_0(x,y)$  into a predefined target intensity distribution  $I_{\text{Target}}(x_l, y_l)$ , where  $(x_l, y_l)$  are the Cartesian coordinates of the calculation grid in the writing plane. Using the GS algorithm as an example of the procedure, with reference to the schematic in Figure 6B, a phase distribution is randomly assigned to the object  $\psi(x,y) = \psi_0(x,y)$ . Then, this phase distribution is combined with the amplitude of the incident light  $E_{\text{in}} = A_0 e^{i\psi} = \sqrt{I_0} e^{i\psi}$  and an initial FFT operation is performed obtaining  $E_{\text{out},1} = \mathcal{F}[E_{\text{in}}] = \tilde{A}_0 e^{i\psi_{\text{out}}}$  ( $\mathcal{F}$  denotes the Fourier transform operation). Consequently, by replacing the resulting amplitude from the FFT with one of the target intensity distributions a new light field  $G = A_{\text{Target}} e^{i\psi_{\text{out}}} = \sqrt{I_{\text{Target}}} e^{i\psi_{\text{out}}}$  is obtained. At this point, the latter will be used to evaluate a given merit function, which characterizes the convergence and accuracy of the algorithm. If after some interaction this merit

function shows no improvement, the phase distribution at the input will be used to generate the CGH, otherwise, the phase information will be retained and the amplitude will again be replaced with that of the incident light to initiate a subsequent iteration until the merit function will show convergence. This merit function can be defined in different manners and can be, for example,<sup>[165]</sup> the root mean square deviation  $\Delta I$  between the intensity at the  $i$ -th iteration,  $I_i(x_1, y_1)$ , and that of target  $I_{\text{Target}}(x_1, y_1)$ :

$$\Delta I = \sqrt{\frac{\iint (I_{\text{Target}}(x_1, y_1) - I_i(x_1, y_1))^2 dx_1 dy_1}{\iint I_{\text{Target}}^2(x_1, y_1) dx_1 dy_1}} \quad (14)$$

Although GS algorithms are the most widely used, finding applications in fields such as imaging,<sup>[166]</sup> encryption,<sup>[167]</sup> and optical tweezers,<sup>[168,169]</sup> there has been no lack of strategies over the years to improve and optimize CGH extraction. These include the Simulated Annealing algorithm,<sup>[170]</sup> among the first to be introduced but also to be somewhat sidelined due to the fact that the algorithm might in principle require an infinite number of iterations. Another example is the Adaptive Additive (AA) algorithm,<sup>[171,172]</sup> in which, after the evaluation of the merit function, the amplitude computed by FFT is replaced with a weighted amplitude of the previous iteration and the target one, given by  $\tilde{A}_i = [a\tilde{A}_{i-1} + (1-a)\tilde{A}_{\text{target}}]$ , where  $a$  represents a certain mixing ratio (if  $a = 1$ , the AA algorithm becomes the GS one). Finally, let us mention the Mixed Region Amplitude Freedom (MRAF) algorithm,<sup>[173,174]</sup> it offers better accuracy than the GS by acting on the initial choice of the phase distribution, which instead of being random is composed of the combination of a linear gradient and a conical gradient, to ensure the absence of so-called optical vortices (points characterized by singularities in the phase distribution and with zero intensity). Other algorithms, for example, the Optimal Rotation Angle (ORA) algorithm,<sup>[175,176]</sup> are called direct Fourier methods, because they do not include IFFT operations.

#### 4.1.3. Optical System Implementation

HoloTPL provides that a CGH can be reproduced on the active area of a modulation device to take advantage of the possibility of reproducing a user-determined intensity distribution on the writing plane from an incident light intensity distribution (uniform plane wave or Gaussian). Here the technological principles on which these devices are built will be concisely introduced and the arrangements used for their integration into a HoloTPL setup will be briefly outlined.

Two wavefront shaping devices are mainly employed: i) digital micromirror devices (DMDs) are micro-opto-mechanical systems consisting of an array of several hundreds of micromirrors (pixels) which can be rotated at a specific angle, locally modifying the reflection of the impinging beam, hence attaining an on/off optical state for each pixel; ii) spatial light modulators (SLMs), which instead can spatially shape phase and/or intensity of a light beam by relying on different technologies, such as deformable micromirrors (DMM), piston-like MEMS systems, or nematic liquid crystal (LC). The two devices are schematized

in Figure 6C. Turtaev et al. compared the performances of the two different classes of devices in light modulation:<sup>[177]</sup> DMDs offered several orders of magnitude faster modulation rates and overall beam-shaping fidelity, while SLMs gave a better modulation depth, diffraction efficiency, and, overall, power efficiency. Based on these considerations, there is not an evident reason to choose one technology over the other, with both offering distinct advantages and drawbacks. DMDs are also less prone to loss channels like pixel crosstalk, which instead can affect LC-SLMs and require proper optimization of the CGH to compensate for it, as discussed by Engström et al. in Ref. [178].

The integration of these devices in a TPL setup follows some general principles, while the adoption of particular details is guided by the specific application. In general, the modulation device imposes a spatial distribution of amplitude and/or phase through a CGH impressed on its surface. The modulation device needs to be placed before the objective lens to modulate the beam and to be optically conjugated to its back focal plane. A representative optical path and its routing are shown in Figure 6D: i) to ensure a good modulation, the impinging beam should cover an active area of the modulation device as large as possible, and for this reason, the beam is typically expanded by a magnifying relay lens arrangement before the device. ii) The DMD or SLM is placed in the optical setup to ensure that a small angle is formed between the impinging beam and the reflected beam, typically less than  $10^\circ$ , while transmissive devices can be placed in an inline arrangement. iii) The optical plane of the modulation device needs to be conjugated with the objective's back aperture, and this is typically obtained by a 4f lenses arrangement configuration that de-magnify the beam to also match the size of the active area of the modulating device with that of the objective entrance pupil, and iv) a blocking element, like a pinhole, is inserted at the Fourier plane of the modulation device to remove the unmodulated zeroth order diffraction.

HoloTPL can also be combined with translation stages to move the sample during the patterning process, or with a galvanometric mirrors pair to scan the projected image. In this latter case, however, larger galvo mirrors are required to host the larger modulated beam, increasing the distance between them, and therefore compromising their virtual conjugation and resulting in a strong vignetting of the writing field of view. To account for the problem, recently Pisanello et al.<sup>[78]</sup> implemented a HoloTPL custom setup that takes advantage of a third galvo mirror, adapting the design proposed by Sofroniew et al.<sup>[181]</sup> in the context of two-photon imaging. The role of the third mirror is to compensate for the beam displacement that compromises the virtual conjugation between the two principal mirrors, obtaining a marked reduction of the vignetting effect, with an overall improvement of a factor  $\approx 2$  of the writing field of view.

By virtue of the modulation device capabilities, the optical setups here described can be dynamically adapted to a series of applications that address different limiting factors of classical TPL, including parallel polymerization of multiple structures, complex shaping of the laser focus, and compensation for optical aberrations. These features can be obtained thanks to the possibility of feeding the modulation devices with proper CGHs.



## 4.2. Phase Modulation for Multifocal Parallel Writing

In multifocal parallel writing, modulation devices produce a partitioning of the incident beam in an engineerable and dynamically reconfigurable fashion, generating arrays of foci in the writing plane, and exploiting a diffractive pattern-based hologram. The use of this technique must ensure control over two factors: i) the laser power incident on the modulation device must be high enough for all individual foci to effectively polymerize the corresponding voxel, and ii) the modulated wavefield must have high uniformity to avoid uneven voxels sizes or mechanical properties of the resulting patterns.<sup>[182]</sup> This is usually addressed by software optimization in the calculation of CGHs, but additional hardware optimization can be also employed.<sup>[183]</sup> Despite a series of static modulation approaches to parallelize the TPL that have been described in Section 3.2, multifoci-HoloTPL provides the possibility to individually control the motion and intensity of each focus in the array, instead

of producing an array with a fixed geometrical arrangement of the relative positions of the foci. Together with the possibility to create multiple replicas of a structure, this approach allows to have multiple voxels contributing to the writing of single pattern.

The multifocal parallel writing was introduced in 2008 by Takahashi et al.<sup>[184]</sup> who, utilizing an ORA algorithm to produce the hologram in **Figure 7A**, demonstrated the generation of 10 diffracted spots from a single laser beam reflected by an LC-SLM (Figure 7B). Here, the SLM projects a static image onto the writing plane while multiple linear structures are polymerized in parallel through sample movement by means of a 3D motorized stage. Multifoci-HoloTPL allows arbitrary arrangement of foci, which can be organized into rectangular<sup>[185]</sup> or hexagonal arrays,<sup>[186]</sup> leading to a high degree of parallelization. An example is in the work of Hasegawa et al.,<sup>[187]</sup> in which simultaneous processing using more than a thousand beams (Figure 7C) was shown (the maximum was 1189 beams

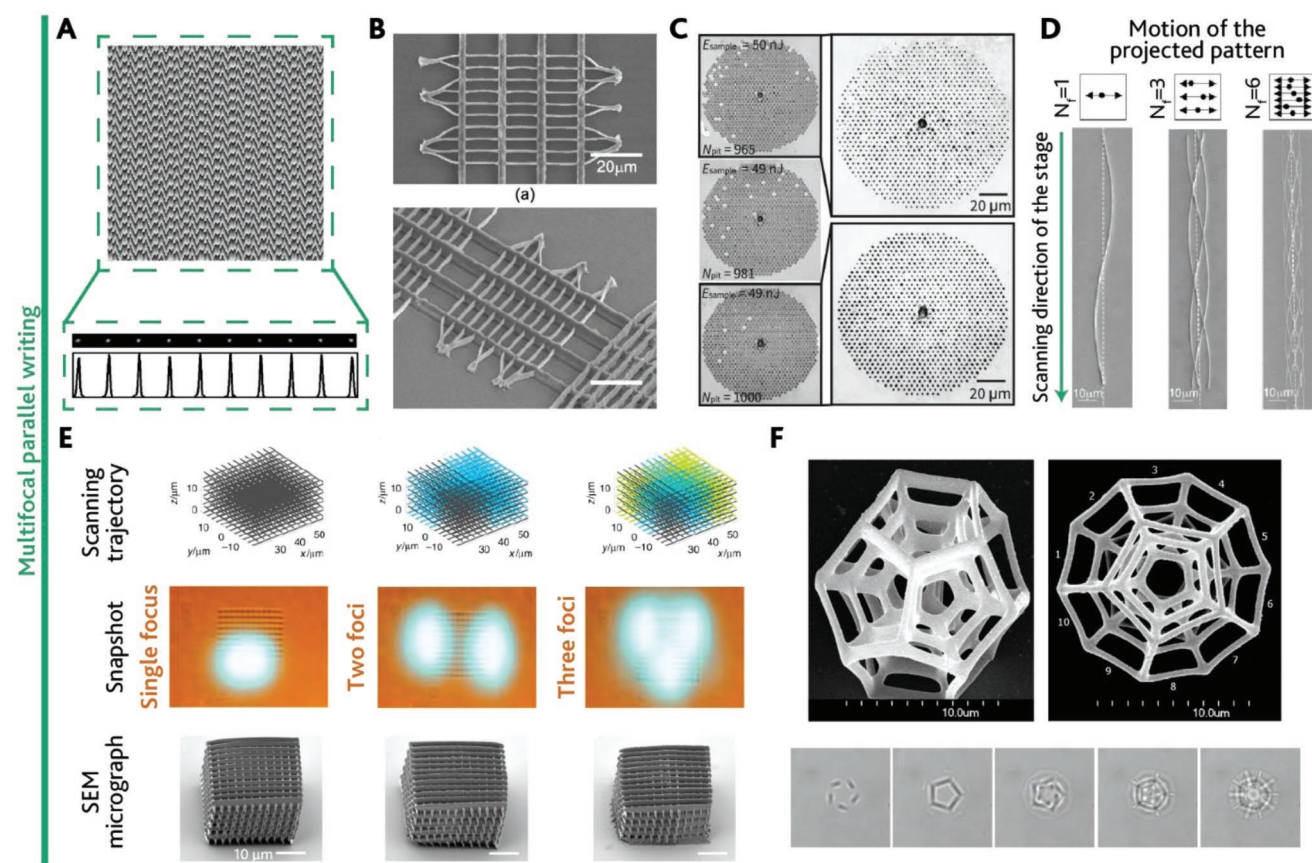


**Figure 7.** A) CGH employed to generate ten foci (top) and the corresponding intensity distribution in the writing plane (bottom). B) SEM images of ten linear structures with four thick supports fabricated with HoloTPL. Panels A and B adapted with permission.<sup>[184]</sup> Copyright 2008, Optical Society of America. C) Massively parallel fabrication of microstructures employing over 1000 CGH-generated foci. The processing was performed with five pulse shots with gradually increasing average pulse energy. Reproduced with permission.<sup>[187]</sup> Copyright 2016, Optical Society of America. D) SEM micrographs of sinusoidal structures fabricated with one, three, and six foci at phase shifts of  $120^\circ$  or  $60^\circ$ , respectively. Reproduced with permission.<sup>[188]</sup> Copyright 2010, Optical Society of America. E) 3D woodpile structures fabricated with one, two, or three individually addressed foci (left, center, and right respectively). (top) Calculations of the laser scanning trajectories, each color represents a different focus, (middle) snapshots of the fabrication process, (bottom) SEM micrographs of the fabricated structures. Reproduced with permission.<sup>[190]</sup> under terms of the CC-BY license. Copyright 2019, The Authors, published by Springer Nature. F) Fabrication of a 3D dodecahedron with 5 independent foci. (top) SEM micrographs of the polymerized 3D structure. (bottom) Sequence of brightfield images of the fabrication process. Adapted with permission.<sup>[192]</sup> Copyright 2014, Optical Society of America.

arranged in a hexagonal structure). This work is an example of the importance that the aforementioned point (ii) can have when large parallelization is implemented: such a high number of simultaneous foci required special CGH retrieval optimizations to account for the inhomogeneity introduced by the optical system.

In 2010 Chichkov's group<sup>[188]</sup> proposed the combination of a series of CGHs supplied to an SLM with a given refresh rate to dynamically control the position of the individual spots during the patterning process, expanding the possibilities offered by the previous work. This was combined with the synchronous movement of a translation stage to realize asymmetrical 2D structures (Figure 7D). 3D geometries were achieved by repetition of the process in different planes (the transition from one plane to the next is enabled by an additional translation stage).

Independent multifoci control in HoloTPL, therefore, allows for a high degree of freedom for the user, allowing to write almost any type of shape at an increased speed factor equal to the number of employed foci. For instance Ritschdorff et al.<sup>[189]</sup> demonstrated simultaneous control over the rastering trajectory of two foci in a 2D plane by a DMD along asymmetrical trajectories, Geng et al.<sup>[190]</sup> used a DMD to independently control 3 foci to make complex woodpile structures (Figure 7E), Papazoglou et al. realized complex 3D hollow structures,<sup>[191]</sup> while Vizsnyiczai et al.<sup>[192]</sup> used a modified version of the weighted GS algorithm to check the 3D position of 5 foci simultaneously, reporting the fabrication of a nested set of dodecahedron frames of decreasing size, each independently cured by the single foci (Figure 7F).

### 4.3. Phase Modulation for Focus Beam Shaping

Another peculiar possibility offered by the conjunction of TPL and holographic methods lies in the ability of controlling the morphology of the focused voxel so that geometries that differ from the ellipsoidal shape returned by classical TPL (Section 2.1) can be polymerized with a single exposure. The holographic techniques that enable this possibility are referred to as "beam shaping techniques". In this section, applications of these strategies will be analyzed in two contexts: i) focal field engineered TPL, consisting in 3D modulation of the intensity distribution to pattern extended structures, far beyond the dimension of the single spot, ii) beam conditioned TPL, exploiting holography for compensating optical aberrations introduced by the optical system.

#### 4.3.1. Focal Field Engineered HoloTPL

CGHs allow to predetermine an intensity distribution in the writing plane and generate the corresponding hologram. This possibility has been widely used in application fields ranging from microfluidics to the fabrication of optical waveguides in transparent materials. There is no shortage of examples of the use of these techniques in the field of HoloTPL as well, with several reports of different Focal Field Engineering (FFE) strategies.

As a demonstration of the versatility of the technology, Yang et al. showed TPP with a single exposure of different arbitrary

patterns,<sup>[193]</sup> such as letters and geometric shapes. Subsequent optimizations by Zhang et al. (2014)<sup>[194]</sup> proposed a multi-CGH exposure by 20 CGHs calculated through GS algorithm, and then Zhang et al. (2016)<sup>[174]</sup> proposed the use of the MRAF algorithm instead of the GS algorithm (Figure 8A), resulting in significant improvements in the quality of single-exposure polymerization, especially in terms of surface quality and reduced influence from speckle patterns, but at the expense of process efficiency, with the fraction of energy used by the GS algorithm hovering  $\approx 65\%$  and that of the MRAF dropping to  $\approx 4\%$ .

One area of interest is to fabricate hollow cylindrical<sup>[195]</sup> or polygonized<sup>[196]</sup> structures by means of FFE strategies. This can be done through CGHs reproducing annular Fresnel lenses, obtained by translation or rotation of a hologram reproducing a Fresnel lens around a fixed point, usually tangent to the lens. This allows target hollow structures to be generated by offering rapid control over their size with a single exposure. In many cases, there may be a need to fabricate structures with high aspect ratios, well beyond the axial extent of the polymerization voxel. For this reason, several studies have focused on the use of Bessel beams<sup>[197]</sup> to engineer the focal field. Bessel beams are waves whose amplitude can be described by a Bessel function. Their main characteristic is their non-diffractive nature, allowing their propagation without diverging after being focused in small volumes. In addition, they are considered self-healing beams, as they can regenerate even if partially obstructed at one point. From the CGH point of view, Bessel beams can be obtained through a phase pattern of the type:<sup>[198,199]</sup>

$$T_n(r, \theta) = e^{in\theta} \cdot e^{-\frac{i2\pi r}{r_0}} \quad (15)$$

in which two terms can be identified: the first controls the azimuthal phase, while the second generates a first-order Bessel function.  $r$  and  $\vartheta$  are the transverse and polar coordinates, respectively,  $n$  is the order of the Bessel function, and  $r_0$  is a constant parameter. Generally, a diffractive grating is combined with this to separate the Bessel beam from the zero-order diffraction. In this way, it is possible to generate annular patterns that are cured by a single exposure with an axial dimension in the order of microns or tens of microns, enabling voxel aspect ratios larger than 40,<sup>[200]</sup> while preserving the typical lateral resolution of TPL, on the order of a few hundred to sub-100 nanometers.<sup>[199,201]</sup> Yang et al.<sup>[202]</sup> have proposed superposition of Bessel beams of different  $\pm n$  order as an alternative strategy for generating multiple foci (Figure 8B, top), through a phase pattern that resembles the one in Equation 15 with an additional factor:

$$T_{\pm n}(r, \theta) = e^{in\theta} \cdot e^{-\frac{i2\pi r}{r_0}} \cdot e^{in\theta(-1)^{1/\Delta}} \quad (16)$$

The hologram is formed by concentric rings with azimuthal modulation and the additional term depends on  $\Delta$ , which represents the width of such rings. By dynamically controlling the separation and rotation angle of the foci as they move along the axial direction, complex 3D patterns can be realized (Figure 8B, bottom). The strategies described above contribute significantly to reducing the time required by the fabrication of such structures compared to traditional TPL, which would require

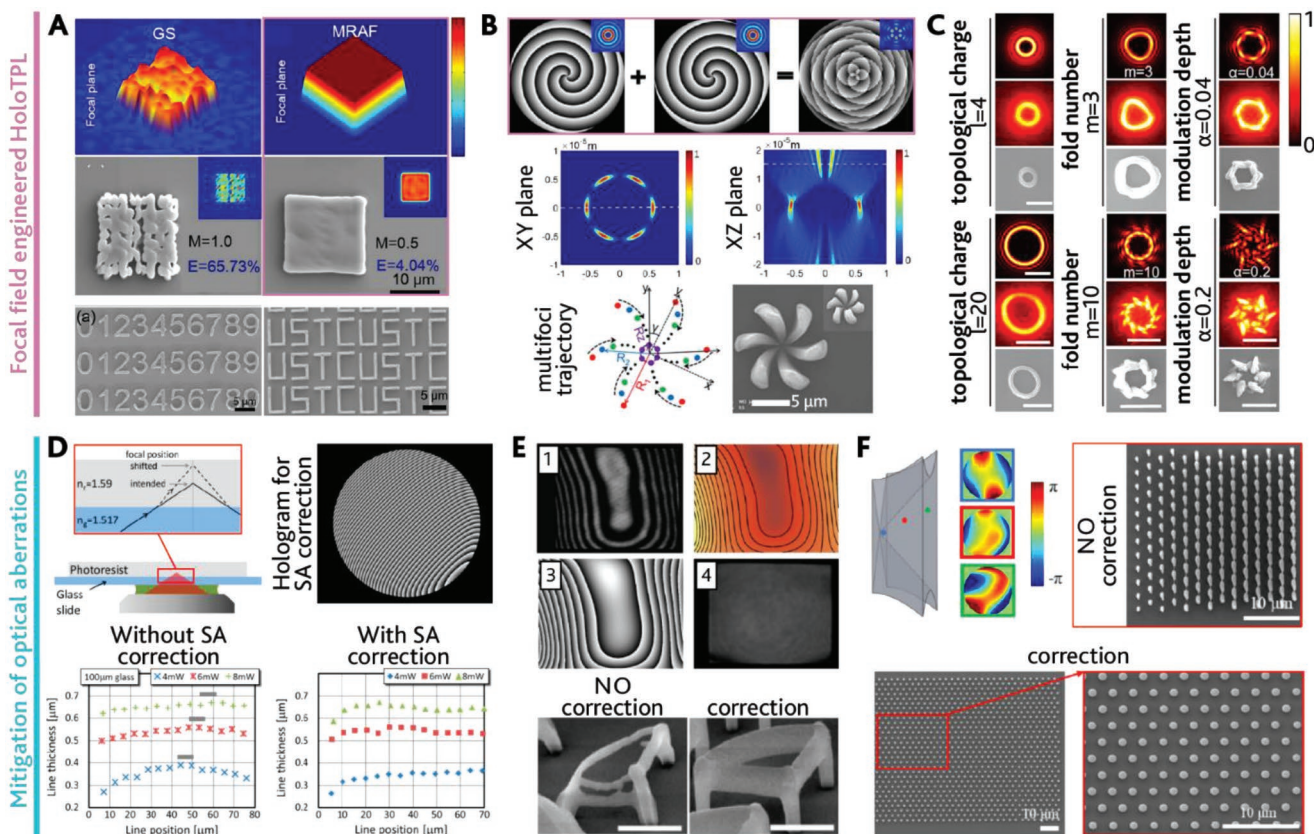


**Figure 8.** A) Generation of a flat-top intensity distribution with CGH evaluated with different algorithms: GS (top-left) and MRAF (top right). (center) SEM images of rectangles fabricated by MRAF-evaluated CGH, with mixing ratio value from 1.0 (left, corresponding to a GS algorithm) to 0.5 (right). The surface quality improves when the  $M$  value decreases. (bottom) SEM images of polymerized numbers (left) or letters (right). Reproduced with permission.<sup>[174]</sup> under terms of the CC-BY license. Copyright 2016, The Authors, published by Springer Nature. B) (top) Generation of superposed Bessel beams by alternatively imprinting holograms of opposite-order Bessel beams (left and center) to generate a composite hologram (right). (center) Intensity distributions in the XY and XZ planes of a superposed Bessel beam. (bottom) Flower-like microstructure fabricated by dynamically controlling the pattern in the focal plane. Reproduced with permission.<sup>[202]</sup> Copyright 2017, Optical Society of America. C) Simulated and measured intensity distribution on the XY plane generated by femtosecond optical vortices with topological charge  $l = 4$  (top) and  $l = 20$  (bottom), and corresponding SEM micrographs of the polymerized structures. The intensity distribution changes depending on fold number  $m$  and modulation depth  $\alpha$ . Reproduced with permission.<sup>[203]</sup> Copyright 2017, AIP Publishing. D) (top-left) Focusing of a laser beam into a photoresist on a glass slide with a high NA objective. This standard writing configuration introduces a refractive index mismatch, and spherical aberrations (SA) with consequent distortion of the voxel. (top-right) Phase-shifting hologram employed to mitigate the spherical aberrations. (bottom) Comparison of line thickness values as a function of the position over the glass from uncorrected lines and SA-corrected lines. Reproduced with permission.<sup>[210]</sup> under terms of the CC-BY license. Copyright 2017, The Authors, published by MDPI. E) Generation of a compensation CGH to compensate for the distortion induced by the SLM screen. (top) Interferogram on the aperture of the SLM, the calculated correcting hologram, and the measured interferogram with the correcting hologram displayed on the SLM. (bottom) Comparison between test structures fabricated with non-corrected and corrected SLM. Reproduced with permission.<sup>[214]</sup> under terms of the CC-BY license. Copyright 2011, The Authors, published by Optica Publishing Group. F) Distortion correction on a DMD. (top-left) Distorted wavefront measured at three different locations in the DMD, (top-right) large area fabrication without the correction method, and (bottom) results of the same fabrication with the correction method. Reproduced with permission.<sup>[216]</sup> Copyright 2021, Optical Society of America under the terms of the OSA Open Access Publishing Agreement.

scanning a single spot along a circular, axially repeated trajectory, consequently increasing throughput. In addition, by virtue of the flexibility given by the generation of CGHs, these holograms can be combined with the diffractive patterns associated with multiple foci generation, so that the advantages of both strategies are combined, while still considering the two basic principles introduced in Section 4.2.

A latest FFE approach consists in controlling the Orbital Angular Momentum (OAM) to obtain optical vortex beams which allow real 3D structuring of the voxel. Indeed, this allows obtaining different axial sections of the voxel similar

but non-homothetic, with a greater number of parameters that can be controlled with respect to Bessel beams<sup>[203]</sup> (topological charge  $l$ , fold number  $m$ , modulation depth  $\alpha$ ), resulting in greater engineering freedom over the structuring of the focus (Figure 8C). The use of optical vortices has been shown to be particularly convenient in fabricating chiral structures, such as double helices,<sup>[204,205]</sup> and complex designs with multiple folds.<sup>[203,206]</sup> Other examples of FFE allowed to obtain complex extended 3D intensity distribution on the writing plane, even without any similarities between different axial sections.<sup>[207]</sup>

#### 4.3.2. Mitigation of Optical Aberrations with HoloTPL

In general, the performance of any optical system can be limited by aberrations introduced by the optical elements on the path, and TPL is not an exception. In high-resolution TPL, high-NA objectives introduce complicated contributions to focal asymmetry,<sup>[208]</sup> while if low-NA lenses are employed axial elongation of the voxel is observed, resulting in a pronounced asymmetry with respect to the transverse direction. In addition, the standard writing configuration involving the use of an oil-immersion objective, a glass slide, and then the resist easily introduces a refractive index mismatch, which results in axial asymmetry of the voxel and severe in-plane asymmetry due to spherical aberration.<sup>[209]</sup> In this context, the use of a modulation device comes in handy, allowing the introduction of spherical phase modulation that is used to pre-compensate for the spherical aberration introduced by the system<sup>[210–212]</sup> (Figure 8D). The axial asymmetry with respect to the transverse direction of the voxel contributes to enlarging the smallest achievable feature size, and HoloTPL can significantly reduce this asymmetry by introducing shaping of the beam using focus field engineering techniques. These allow a nearly spherical voxel to be realized while compensating for spherical aberrations by combining a CGH for spherical phase modulation with a slit-shaped mask on the active area of a modulating device.<sup>[208,213]</sup>

Despite the clear contribution made by modulation devices in reducing these aberrations and asymmetries, the modulation device itself can be a source of aberrations, as shown by Kelemen et al.<sup>[214]</sup> (Figure 8E) who studied the surface distortion induced by an SLM on the wavefront and proposed a correction strategy, which consists in generating a compensation CGH, calculated starting from the interferogram measured at the SLM surface. HoloTPL may suffer from spatial dispersion of wavelengths due to the diffractive effect of the SLM on the incident beam, especially when femtosecond pulses with wide bandwidth are used. This leads to the onset of chromatic dispersion that further elongates the voxel in the axial direction, which becomes more pronounced for shorter pulses. This effect can be compensated, for example, by using a second SLMs introducing symmetric wavelength-dependent angular separation.<sup>[215]</sup> Most of the compensation methods described so far aim for global average correction over the entire workspace, although aberrations related to modulation devices are typically local in nature and not uniform over the active area. Through a local correction, obtained by evaluating the distortion induced by separate subregions of a DMD, Ren et al.<sup>[216]</sup> achieved efficient voxel optimization and uniformity over the fabrication FOV, resulting in aberration-free large-area stitch-free 3D structures with total dimensions of hundreds of micrometers (Figure 8F).

Optical aberration mitigation strategies are critical when HoloTPL is used at the limits of its resolution. However, for the time being, many of the studies available in literature set out to study new manufacturing strategies without taking these factors into account, as HoloTPL is still going through a period of intense research and development, having been introduced just over a decade ago. Salter and Booth<sup>[217]</sup> recently offered a comprehensive review of the use of modulation devices in laser processing, not limited only to HoloTPL, providing an extensive

overview of the optical aberration mitigation strategies in different contexts.

## 5. Applications of HoloTPL

The previous section describes how HoloTPL enabled the development of a variety of strategies aimed at increasing throughput and, more in general, engineering degrees of freedom in TPL. Parallelization strategies through replication of multiple foci, combined with the usual scanning techniques (galvanometric mirrors, motorized stages) allowed simultaneous polymerization of dozens of structures; FFE beam shaping, alternately, made it possible to obtain extended structures with complex 3D geometries with a single exposure. The flexibility offered by HoloTPL allows the two approaches to be combined to replicate complex structures simultaneously, without the need to use scanning techniques. The scientific community has thus made use of the tools described in Section 4 in a multitude of different fields, ranging (but not limited) from optics, and photonics, through microfluidics, cell biology applications, and micromachines. Below, a series of papers, divided by research topic, that have taken advantage of the remarkable capabilities of HoloTPL are reported.

### 5.1. HoloTPL in Microfluidics

Microfluidics and lab-on-chip systems are employed in many application fields, spanning from physics and biology to medicine and pharmaceuticals, exploiting the advantage of small dimensions, minimized reagent consumption, and offering the possibility to integrate microdevices to achieve additional functionalities such as particle sorting and cell filtering.<sup>[218]</sup> In this context, HoloTPL can be a more versatile technique than UV Lithography and Nanoimprinting Lithography, as it does not require additional masks or molds. If compared with conventional TPL, in particular cases it can result in an increased process speed: if patterns are composed by simple 2D elements, HoloTPL based on FFE does not require a point-by-point scanning strategy to realize them, while even if complex 3D structures must be fabricated, the multifoci approach allows to use a point-by-point scanning strategy in parallel over multiple patterns.

Most HoloTPL applications in the field of microfluidics aim at the realization of particle and cell sorting/filtering<sup>[219,220]</sup> structures, which are of great importance for cell sequencing, drug screening, and purification of bio-samples. One of the first implementations of HoloTPL in this aspect was proposed by Zhang et al.<sup>[174]</sup> in 2016. In the work, the authors exploited FFE with an MRAF-based CGH to fabricate a large-area array (5000 × 170 μm) of V-shaped grooves into the microfluidic channel for SiO<sub>2</sub> particles capture and separation, in a fabrication time shorter than 10 s.

A work by Xu et al. (2016), reported in **Figure 9A**, proposes the use of an SLM to generate five or seven foci scanning to fabricate a barrier with micro-holes (spanning from ≈3 to 13 μm diameter) in a Y-shaped microchannel to filter breast cancer cells, reducing the fabrication time from 75 to 15 min.<sup>[221]</sup>

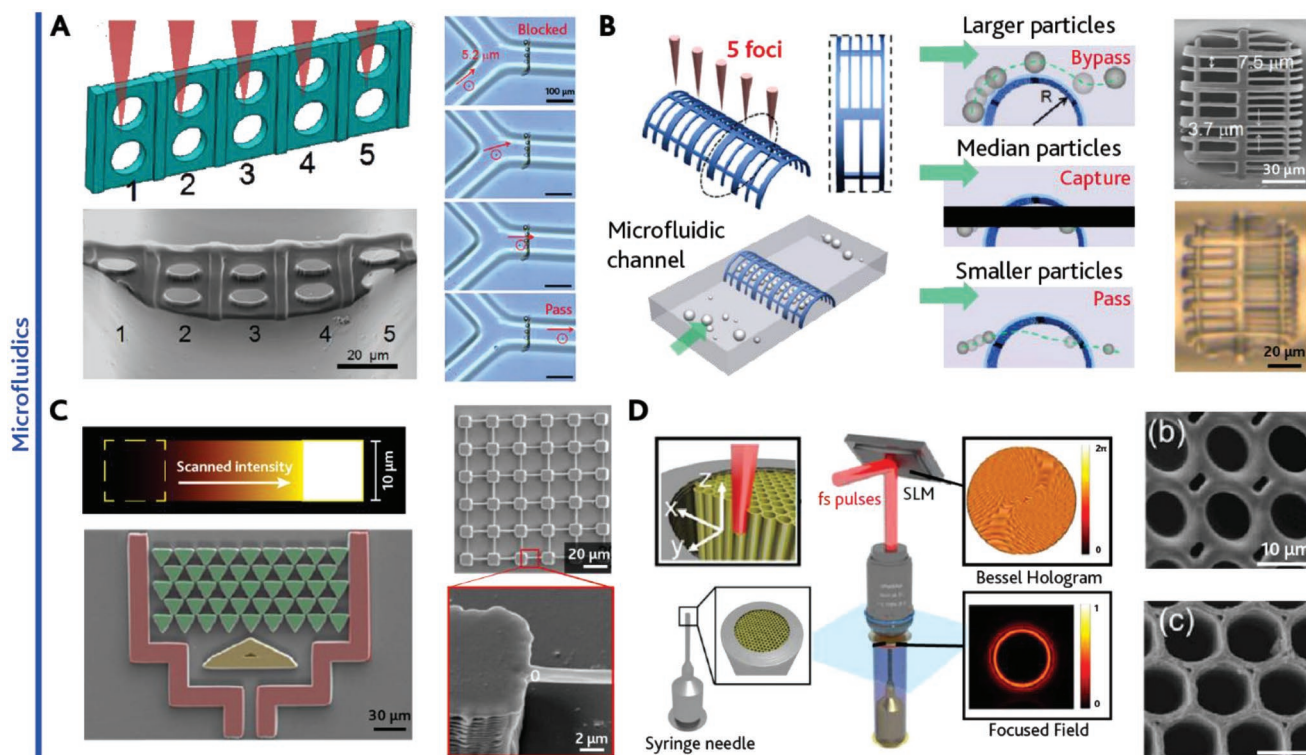


**Figure 9.** A) (left) Schematic representation of a microfilter fabricated with five foci. (bottom) SEM micrograph of the corresponding microfilter inside the microfluidic channel. (right) Snapshot sequence showing a  $2.8 \mu\text{m}$  particle passing through the microfilter easily, while larger particles are blocked. Adapted with permission.<sup>[221]</sup> under terms of the CC-BY license. Copyright 2016, The Authors, published by Springer Nature. B) (left) Sketch of the arch-like particle sorter and its integration in the microchannel. (center) Schematic of the band-capture sorting mode: the larger particles bypass the sorter, smaller ones pass through the sorter, while the median particles are captured in the polymeric structure. (right) SEM micrograph of the final sorter for  $5 \mu\text{m}$  particle, and optical image of the sorter immersed in water. Adapted with permission.<sup>[222]</sup> Copyright 2017, Optical Society of America. C) (top) Sketch of the square intensity distribution scanned in the focal plane. (bottom) SEM image of a particle trapper fabricated with different patterned foci, marked in red, yellow, and green. (right) Example of structure in which the square pillars are fabricated with a square patterned focus, while the finer structures (shown in the inset) are fabricated with conventional TPL for better accuracy. Reproduced with permission.<sup>[224]</sup> Copyright 2020, Optical Society of America. D) (left) Sketch describing the fabrication of the microfilters inside the needle of a syringe. The Inset shows the CGH on the SLM plane, the intensity distribution on the writing plane, and the fabrication of the micro-cylinders with the resulting Bessel beams. (right) SEM micrographs of different patterns fabricated inside the syringe needle. Adapted with permission.<sup>[226]</sup> Copyright 2019, Optical Society of America.

Concerning particle sorting, Xu et al. (2017)<sup>[222]</sup> proposed a novel architecture to perform multi-modal sorting, consisting of an arch-like shape with different filter sizing, fabricated in a Y-channel (Figure 9B). The authors employed an SLM fed with GS-evaluated CGHs to generate 5 foci in the writing plane to parallelize the writing of the arch structure. The fabrication time of the entire device was about 30 min, much shorter than conventional single femtosecond laser polymerization. HoloTPL was also employed to integrate pH-sensitive arrays of micro-cylinders into a microfluidic channel to fabricate a particle trap device that exploits passive hydrodynamics forces.<sup>[223]</sup> The micro-cylinders, which can swell or shrink depending on the pH in a quick response, were fabricated by generating a Bessel beam with an SLM and exposing SU-8 2025 photoresist. The use of HoloTPL allowed an increase in fabrication speed of  $\approx 10^2$  times. In many implementations of HoloTPL, structured beams are only employed to fabricate the microstructures, while the channel itself is fabricated beforehand using more conventional techniques, such as mask-based UV lithography. In a recent work by Zhang et al.,<sup>[224]</sup> an SLM was employed to generate several, tightly spaced multifoci, to create a square

flat-top intensity distribution on the writing plane, which can be scanned using a translational stage to define the external walls of the microfluidic channel. The microstructuring of the inner-channel region was carried out by generating intensity distributions with different shapes, or by employing a reduced number of foci for the realization of finer structures (Figure 9C). The authors reported a fabrication efficiency higher than  $\approx 20$  times for the fabrication of the channel, and  $\approx 23$  times for the microfluidic filter, moreover these values could be further improved by using a laser source with higher power. The Sugioka group proposed a hybrid TPL / HoloTPL method.<sup>[225]</sup> The authors exploited an approach similar to the previously discussed work to holographically generate a  $10 \times 10 \mu\text{m}$  flat-top intensity distribution, to fabricate a microchannel structure with a relatively low precision in a short time, then they employed conventional TPL to fabricate small, bracket-shaped particle traps in the inner region of the channel with a higher precision. With this combination, a 100% particle-trapping retention rate was achieved, while simultaneously reducing the fabrication time from 17 to 1 h. A non-conventional application is reported in the work of Ji et al.,<sup>[226]</sup> in which HoloTPL was employed to fabricate a

microtube array for particle separation in a syringe needle, a solution which was referred to as lab-in-a-needle concept device (Figure 9D). The authors modulated a Gaussian beam into a ring Bessel beam using an SLM loaded with Bessel CGHs, to fabricate an array of micro-cylinders with diameters ranging from 1 to 10  $\mu\text{m}$ , in a processing time of 4 min. In the proof-of-concept experiment, a 0.5 mL mixture of 2.5 and 20  $\mu\text{m}$   $\text{SiO}_2$  microspheres was filtered by the microstructured needle, resulting in 0.05 mL of monodisperse filtrate containing only 2.5  $\mu\text{m}$  particles.

## 5.2. HoloTPL in Scaffolds for Cells Culture

Conventional TPL has found wide use in the fabrication of polymeric scaffolds for cell culture, which provides the structural support for cell attachment, subsequent tissue development, and study of migration properties of both healthy and tumorigenic cells.<sup>[227,228]</sup> In this context, a large number of samples is essential for interfacing with the correct number of cultured cells relevant for clinical applications, or to build sufficient statistics for confirming or rejecting research hypotheses.

HoloTPL allows speeding up the fabrication through the exploitation of multifoci to write different parts of a single structure in parallel, or to define peculiar geometries through FFE or the use of special beams. Zandrini et al.<sup>[229]</sup> employed HoloTPL to fabricate biocompatible scaffolds for stem cell growth, defined as nichoids, using 6 foci generated with GS-evaluated CGHs. With this multifoci approach it was possible to fabricate a  $5 \times 5$  array of nichoids in just 38 s. Moreover, the authors showed that cell adhesion and proliferation are not affected by the different mechanical properties of nichoids fabricated with a single or multiple foci. Another HoloTPL approach, proposed by J. Chu's group,<sup>[230]</sup> exploited dynamic multifoci to fabricate arrays of pH-sensitive microcages for particle trapping, as well as scaffolds for HeLa cells which can be loaded with drugs for test treatment. The pH-sensitive scaffolds, reported

in Figure 10A, were fabricated with six foci arranged in a hexagonal geometry, and a 14  $\mu\text{m}$  inscribed circle, which can extend to 27  $\mu\text{m}$  in the culture medium to provide enough space for cell settlement. The cellular growth and migration processes were observed as a function of the pH of the culture medium, which causes the scaffold to shrink or expand reversibly.

Special beams were also employed to quickly fabricate scaffolds that meet specific structural needs. Ji et al.<sup>[231]</sup> fabricated microtubes arrays with variable cross sections and different inner and outer diameters for yeast culture. To control the shape of the microtubes, the Gaussian beam impinging on the SLM beam was dynamically modulated by the CGHs to form different types of Bessel beams (BBs) on the writing plane, to fabricate cylindrical, conical, and drum-shaped microtubes (Figure 10B), depending on the topological charge encoded in the CGHs. The yeast cells, captured into the microtubes by capillary force, reached a retention and survival rate up to 70%. Pan et al.<sup>[232]</sup> proposed the use of C-shaped BBs to expose the resist with a gap-ring-shaped intensity distribution. By dynamically rotating this pattern using CGHs, the authors reported the fabrication of microtubes with different cross section geometries (trefoil-, clover-, and spiral-shaped). With this solution, the authors fabricated biomimetic artificial plant stomata which can open and close in a few seconds mimicking the function of the natural cells, by taking advantage of the SZ2080 photoresist, which can deform reversibly after soaking in a polar solution. Further implementations of the FFE were proposed by Wang et al.,<sup>[233]</sup> which employed HoloTPL to generate Mathieu beams (MBs) in the resist, special non-diffractive beams which can be tailored to exhibit a different number of intensity maxima along the azimuthal direction of a transverse plane. By dynamically changing the CGHs, the authors could generate MBs with different numbers of maxima in the azimuthal direction (from 1, corresponding to a BB, to 8), to fabricate 3D microcages with different geometries in less than one second (Figure 10C). The microcages were employed for trapping and culturing yeast cells.

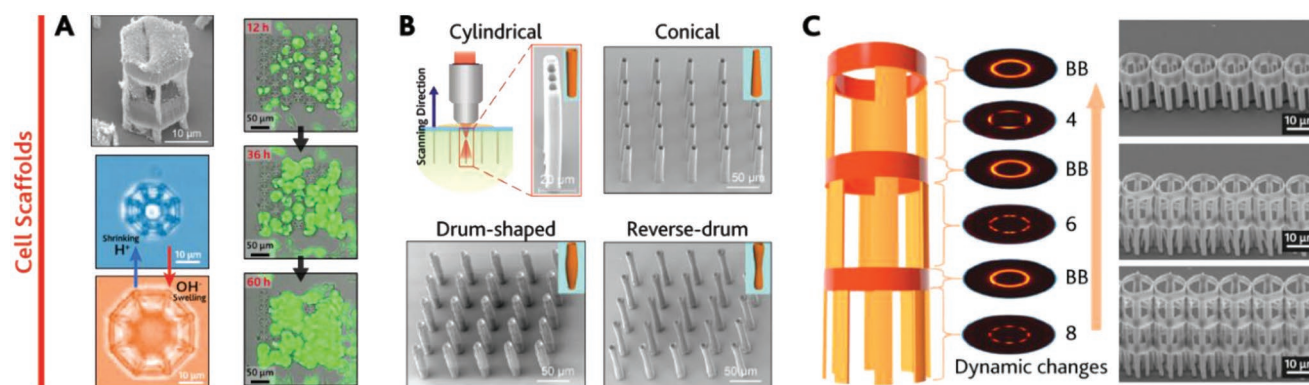


**Figure 10.** A) (top-left) SEM image of HeLa cells growing inside the scaffold. (bottom-left) Optical images showing the swelling and shrinking of a microcage upon a variation of pH of the culture medium. (right) Sequence snapshots of the scaffold array with a culture of HeLa cells inside. Overlay of a bright field image (grey) and a fluorescence image (green). Adapted with permission.<sup>[230]</sup> Copyright 2022, American Chemical Society. B) Schematic illustration of the holographic processing of a cylindrical microtube array, and SEM images of arrays with cylindrical, conical drum, and reverse-drum shapes. Adapted with permission.<sup>[231]</sup> Copyright 2017, Wiley-VCH GmbH. C) (left) Sketch of the fabrication of a three-layer microcage, each layer is fabricated using BBs or different types of MBs. (right) SEM micrographs of different kinds of microcages. Reproduced with permission.<sup>[233]</sup> Copyright 2019, American Chemical Society.

### 5.3. HoloTPL in Microactuators and Micromachines Fabrication

Microactuators are micrometer-sized structures or devices that exhibit mechanical deformation or movement as a result of an external stimulus, which can be of various types.<sup>[234]</sup> These micro-objects have attracted much interest because of their potential applications in a wide variety of areas, including bio/chemical sensing, precision medicine, and biomimetic micro-robotics. For microactuators prototyping, HoloTPL-enabled capabilities are often combined with photoresist engineering, to tailor the properties of the resulting structures in terms of the pH responsivity, mechanical properties, or motion under an external magnetic field.

Li et al.<sup>[235]</sup> developed a TPL-curable hydrogel that shows shrinking or expansion depending on the pH of the environment, patterned with Bessel beams to obtain micropillars that change shape depending on the external pH. Since the magnitude of the pH response also depends on the power of the

curing beam, the authors used asymmetric Bessel beams to obtain polymorphic microtubes (**Figure 11A,B**), arranged in a square or hexagonal lattice to make pH-controllable cells micro-grippers. This can be also combined with compressed phase depth Bessel beams,<sup>[236]</sup> which allows to dynamically modify the diameter of the microtube along its vertical axis, to obtain even more complex polymorphic behavior.

A series of works, instead, combined HoloTPL with different ways to obtain a resist for TPL that showed magnetic properties after polymerization. This makes it possible to create microstructures that can be moved by the application of an external magnetic field so that they can be used as micromotors and as microcargos for drug delivery. In this regard, Xin et al.<sup>[237]</sup> have made hollow microhelices from a TPL-curable sol-gel, using optical vortex beams combined with 3D sample handling (**Figure 11C**). Sputtering a ferromagnetic layer of nickel allowed these to be guided and steered by three pairs of Helmholtz coils in 3D space, which provide a homogeneous 3D rotating

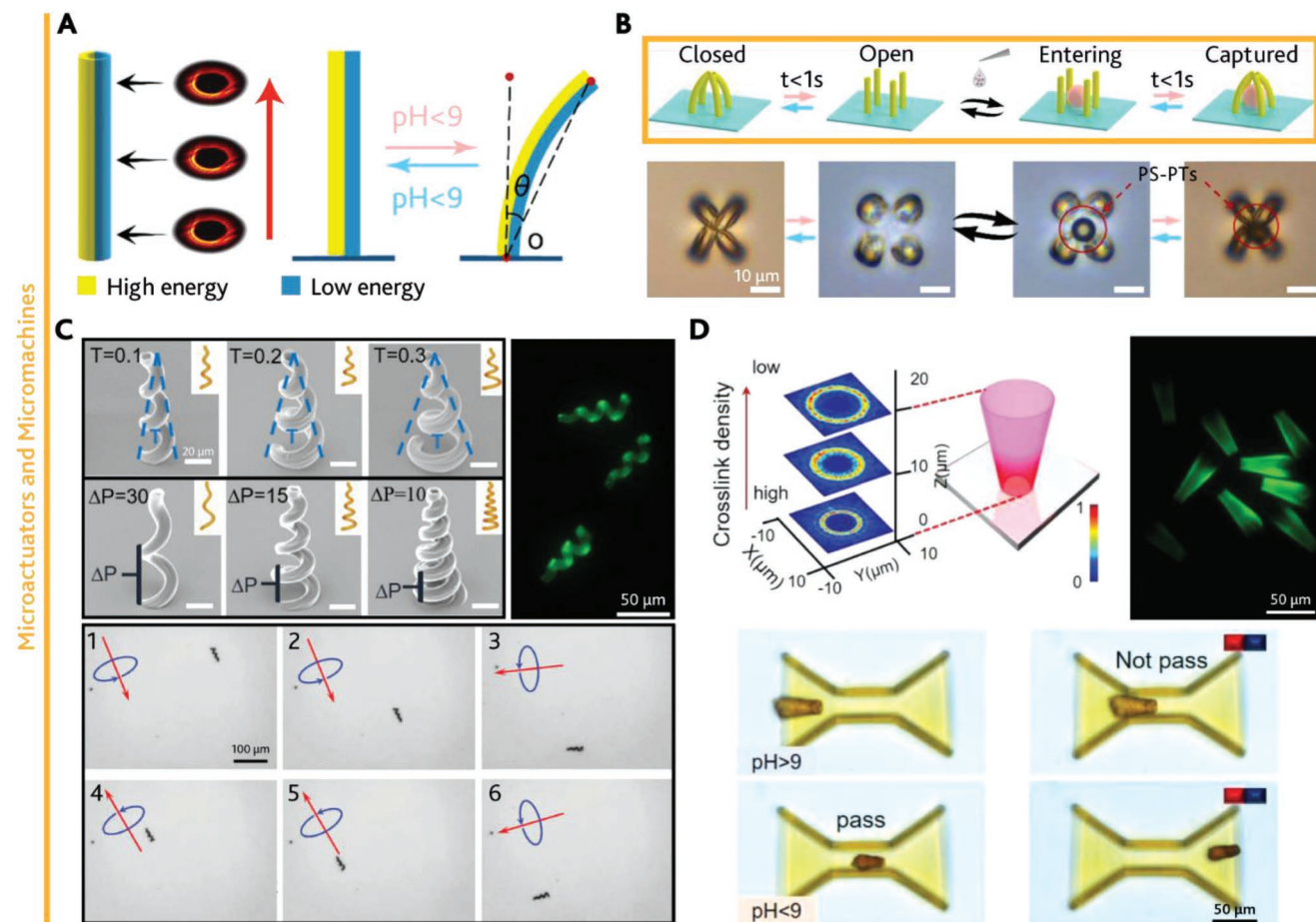


**Figure 11.** A) Sketch of a pH-sensitive microtube fabricated with a modulated Bessel beam. The structure can bend by an angle  $\theta$  depending on the pH of the medium. B) (top) Representation of pH-responsive gripper with four fingers. (bottom) Optical images showing the capture process of a polystyrene particle (PS-PT). Panels A and B adapted with permission.<sup>[235]</sup> Copyright 2020, American Chemical Society. C) 3D hollow microhelices fabricated with HoloTPL. (top-left) SEM of microhelices with different taper angles  $T = 0.1, 0.2,$  and  $0.3$  radians or pitch periods  $\Delta P = 30, 15,$  and  $10 \mu\text{m}$ . (top-right) Fluorescence image of microhelices on the glass substrate. (bottom) Sequence of optical images of a conical microhelix steered in arbitrary direction following the direction of the external magnetic field. Adapted with permission.<sup>[237]</sup> Copyright 2019, Wiley-VCH GmbH. D) Shape-morphing TSMM fabricated by gradient optical vortices. (top-left) Simulated intensity distribution of different cross sections of the 3D optical vortex. A larger light field pattern results in a reduced intensity distribution and weaker polymerization. (top-right) Fluorescence image of hollow TSMM. (bottom) Timelapse sequence of magnetic TSMM passing through an hourglass-shaped microchannel. Adapted with permission.<sup>[239]</sup> Copyright 2022, Wiley-VCH GmbH.

magnetic field. The authors offered a proof of concept of transportation of single and double neural stem cells by the microhelices in vitro, anticipating that these cells can be transported in vivo for cell delivery and damaged tissue repair in future. In a further work,<sup>[238]</sup> the group proposed a similar approach, this time directly using a magnetic TPL resist, produced by mixing a commercial resist with surface-modified Fe<sub>3</sub>O<sub>4</sub> particles. In this case, they demonstrated the fabrication of magnetically propelled hollow microtubes, used for targeted delivery of HeLa Cells and Doxorubicin drug particles for therapeutic applications. Very recently,<sup>[239]</sup> properties of pH-sensitivity and magnetically driven handling have been combined with fabrication exploiting optical vortex beams of hollow trumpet-shaped micromachines (TSMM), employing a pH-sensitive resist, then incubated in a suspension of Fe<sub>3</sub>O<sub>4</sub> nanoparticles (Figure 11D). Through modification of their size controlled by pH and handling by magnetic field, these structures can shrink and pass through channels narrower than their original size and can be guided along microchannels of complex shapes, with bends, constrictions, and barriers, further increasing their adaptability to the environment. These can be modified to handle a diverse range of loads, including therapeutic drugs and diagnostic probes, which are expected to become widely used in the complex micro-networks of biomedicine.

#### 5.4. HoloTPL in Optics and Photonics

In many cases, HoloTPL has been used for prototyping different types of optical and photonic structures. The parallelization capabilities make it possible to dramatically reduce the time required to fabricate complex structures while maintaining the high resolution offered by TPL. In the following, some examples of such applications will be offered, including microlenses prototyping and the realization of structures that exhibit a chiral response.

Hu et al.<sup>[240]</sup> used the multifoci approach to fabricate closely packed arrays of aspherical microlenses with tailored vertex radii (Figure 12A). Through a hexagonal lattice of 64 foci, they concluded the fabrication of the array in  $\approx 20$  min, to be compared with the more than 10 h required by the one-at-a-time fabrication strategy. A similar result was demonstrated by Yang et al.,<sup>[186]</sup> who also extended the fabrication method to other kinds of microphotonic architectures such as 3D woodpile or spiral photonic structures, estimating a reduction in fabrication time that virtually corresponds to the number of foci, net of a slowing of the writing speed to compensate for the lower power available to each focus. Beam shaping techniques enabled by HoloTPL have been used in the fabrication of micro-lenses with complex profiles. An example is the work of Yan et al.,<sup>[241]</sup> in which Fresnel lenses were fabricated by 3D FFE (Figure 12B). The structure was divided into 2D slices in the direction parallel to the incident beam, and each of the slices was used to engineer the focal field. By scanning the engineered focal field in the transverse direction, continuous Fresnel lens arrays were obtained, and fabrication of each lens took just under 7 s, a reduction of at least one order of magnitude compared with conventional TPL (thermal annealing was required to improve the surface quality of the lenses). A 3D FFE approach has also

been implemented by Yang et al.<sup>[207]</sup> to demonstrate the fabrication of microlenses to generate vortex beams with orbital angular momentum of  $l = 0, 1, 2, 3$ , and  $8h$  at a wavelength of 632.8 nm (Figure 12C). Pan et al.<sup>[242]</sup> used a different strategy to obtain an ordered array of microlenses, using a long depth of focus beam. In this way, they fabricated an array of high aspect ratio (HAR) pillars with a height of 15  $\mu\text{m}$ , obtaining each pillar with a single exposure. The ordered array of HAR pillars was employed for micro trapping of SiO<sub>2</sub> microspheres, which function as microlenses. The authors estimated a reduction in writing time by a factor of 50 to 200, depending on the writing parameters used.

3D FFE was employed by Yang et al.<sup>[204]</sup> to fabricate polarization-dependent optical surfaces. This was done by generating orbital angular momentum beam able to perform one-shot-exposure of double microhelices in a time as short as 0.1 s (Figure 12D). An array was then obtained by successive movement of the sample in the transverse plane relative to the incident beam. Following a sputtering deposition of a 30 nm-thick gold layer, the array exhibits a reflectance of 75% or 53% depending on the incident beam left- or right-handed circular polarization, respectively. Further engineering of CGHs can lead to the production of the interference between a vortex beam with a certain topological charge and a plane wave or to annular vortex beams,<sup>[206]</sup> which exhibit a doughnut-like intensity distribution. These beams are used for one-shot fabrication of 3D chiral structures in isotropic materials, and the combination of this technique with high-power industrial lasers can lead to the fabrication of a 1 cm<sup>2</sup> chiral metasurface in  $\approx 5$  min, as opposed to the hours currently required. Pan et al.<sup>[243]</sup> combined HoloTPL optical vortex beam with capillary-force-assisted self-assembly for efficiently yielding chiral microstructures. HoloTPL is used to polymerize a structure composed of multiple lobes in a single step. Following resist development in a liquid environment and subsequent drying in air, a meniscus is formed within the structure which, by exerting a capillary force on the structure results in a folding of the multiple lobes into a more complex structure (Figure 12E). An array of such structures shows an obvious property of vortex dichroism, which is the differential reflection of the incident vortex beams with opposite OAM modes on chiral microstructures. Liu<sup>[244]</sup> suggested a clever solution for rapid prototyping of 3D metal chiral structures by exploiting the principle of multi-step photoreduction of metal ions in an aqueous solution (Figure 12F). Although different from the TPP process, this application also makes use of beam shaping via FFE to produce a double helix voxel to simultaneously photo-reduce a freestanding 3D silver double-helix microstructure without scanning. The produced array of microhelices exhibits pronounced transmission distinction for the left circular polarized and the right circular polarized light in a wide wavelength range from 3.5 to 8.5  $\mu\text{m}$ .

## 6. Conclusions and Outlook

Since its first experimental demonstration, Two-Photon Lithography (TPL) has been a game-changer for the field of Direct Laser Writing (DLW). Together with the possibility to produce 3D structures, the quadratic dependence of the absorption rate



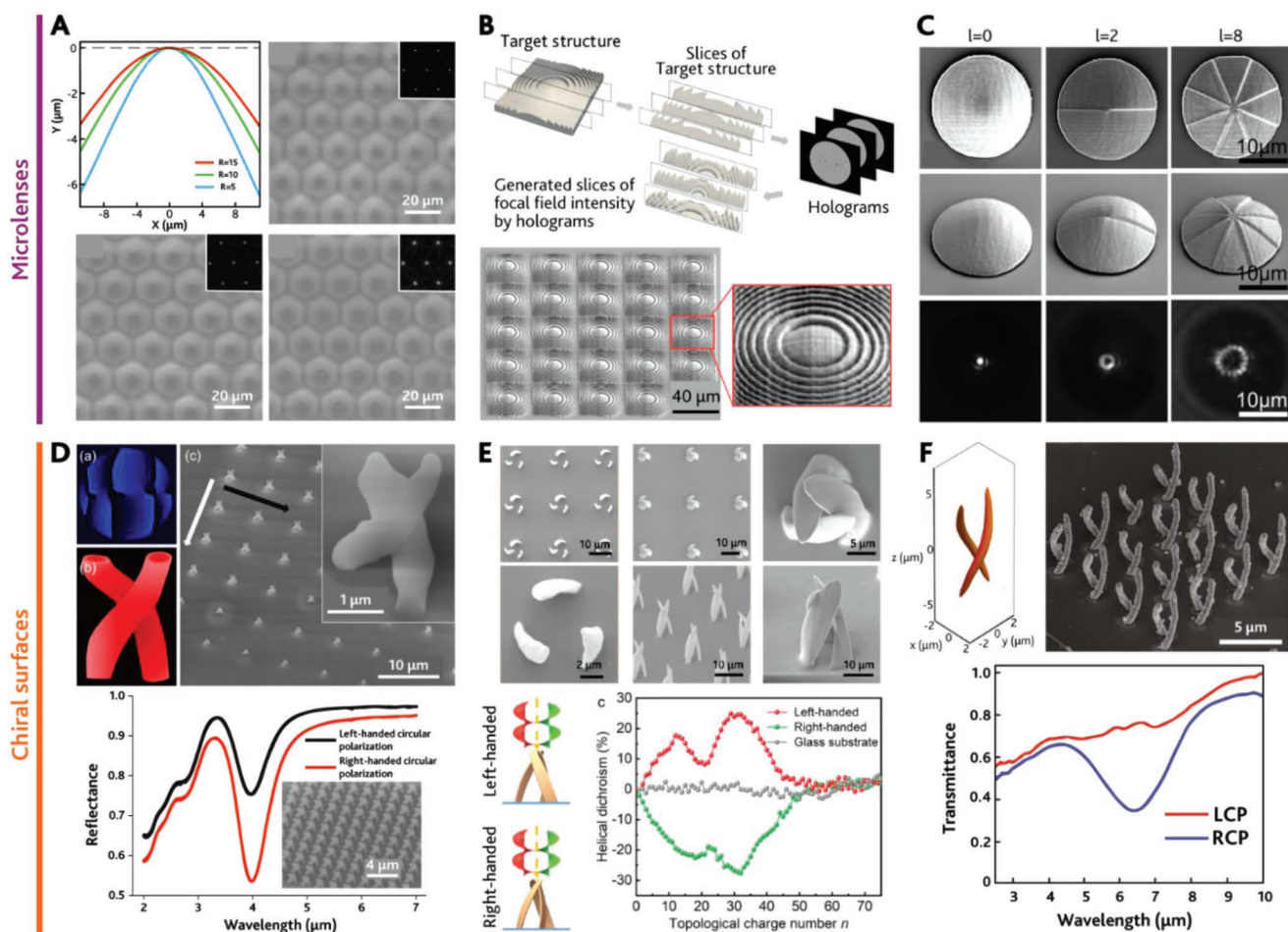


**Figure 12.** A) (top-left) Calculated profile for aspheric lens geometry with different vertex radii. SEM micrographs of closely packed aspheric microlenses arrays (AMLA) with vertex radii of 5, 10, and 15  $\mu\text{m}$ . The insets are focal spots images under illumination by a halogen lamp. Adapted with permission.<sup>[240]</sup> Copyright 2013, AIP Publishing. B) (top) Schematics of the flow chart of 2D sliced focal field intensity profiles generated by holograms calculated by the slices of the target structure. (bottom) SEM micrograph of the 45° tilted side view of the Fresnel lens array annealed at 130 °C. Inset is the magnified image of one lens in the array. Adapted with permission.<sup>[241]</sup> under terms of the CC-BY license. Copyright 2020, The Authors, published by MDPI. C) (top) SEM micrographs of the microlenses that generate vortex beams with different orbital angular momentums. (bottom) Experimental focusing properties under illumination by a halogen lamp. Adapted with permission.<sup>[207]</sup> Copyright 2019, Wiley-VCH GmbH. D) (top-left) Phase mask and intensity plot for a 3D double-helix focus. (top-right) SEM micrograph of the double-helix structures polymerized using different exposure times, along the white arrow, and different heights above the substrate, along the black one. (bottom) Measured reflectance difference between left- and right-handed circular polarizations for a gold-coated array of double-helix structures. Inset is the SEM micrograph of the measured array. Adapted with permission.<sup>[204]</sup> Copyright 2014, AIP Publishing. E) Results of the 3D chiral microstructures fabrication through optical vortex beams (top) SEM micrographs of (left) top view of three-fold chiral structures before the capillary-force-assisted self-assembly and (right) top and side view of the structures after the self-assembly. (bottom) Measured vortex dichroism response on 3D chiral assemblies with opposite chirality and glass substrate. Adapted with permission.<sup>[243]</sup> Copyright 2021, Wiley-VCH GmbH. F) (top-left) The double-helix focal intensity distribution and (top-right) SEM micrographs of silver double helix with double-helix beam superposed obtained by two-photon photoreduction. (bottom) The measured transmittances of the double-helix silver array for LCP and RCP light at normal incidence. Adapted with permission.<sup>[244]</sup> Copyright 2012, Walter de Gruyter and Company.

on the beam intensity quickly enabled TPL to achieve a minimum feature size below the diffraction limit, an insurmountable limit for competing techniques such as UV Lithography, Nanoimprinting Lithography and the like. The introduction of increasingly powerful lasers and more precise and reliable nanometer handling systems has then generated a strong technical advance, resulting in a swarm of technology reports demonstrating the most diverse applications in an ever-widening range of topics. Nevertheless, TPL is essentially a serial technique, in which each device is processed individually, with fabrication times that can take up to several hours if a number of

parameters are not optimized. This makes it difficult to define an industry standard for the fabrication time as the throughput of the process strictly depends on the type of device to be fabricated.

In general, a throughput increase can be achieved by working on several fronts. First, by optimizing the chemical and physical properties of the photoresist, adopting resins with a good dynamic range and a high radical quantum yield, so that a good number of radical species can be generated without damaging the resist. A second important aspect is the type of scan used: translational stages and galvanometric scanners

have inherent pros and cons, and the combination of both technologies can make the lithography system more versatile and faster, as well as reduce imperfections due to stitching of individual patterns. Other solutions reported in literature exploit the combination of one-photon and two-photon processes, in which structural parts are fabricated with one-photon exposure, while finer details are written with TPL. Conversely, other solutions involve defining the structure shell by TPL, followed by UV curing of the internal domain, to reduce the processing time. The parallelization methods discussed in Section 3.2 can offer a tremendous boost to the final yield of the process; however, they are not applicable in every context. The use of transparency masks combined with spatiotemporal focusing allows the fabrication of complex 2D patterns with a single exposure, but they are poorly employable to produce multiple identical structures in parallel. In contrast, the use of microlenses arrays or phase masks allows increasing the number of micro-objects fabricated in parallel, but their application is limited to periodic structures. The employment of microtransfer molding, on the other hand, allows for large-scale translation of complex 3D structures, but the inherent topological limitations must be considered.

Concurrently, the scientific community is exploring the combination of the advantages of high resolution and 3D prototyping offered by TPL with the dynamic structuring of the intensity distribution on the writing plane provided by holography, which we have referred to in this paper as “HoloTPL”. In particular, technological developments in the field of light wavefront modulation devices, such as Spatial Light Modulators (SLM) and Digital Micromirror Devices (DMD), together with more powerful lasers, have made it possible on the one hand to introduce a certain degree of parallelization of lithographic processes, through the multifoci approach, and on the other hand to obtain complex 3D structures with a single exposure, through focal field engineering techniques. There is no doubt that the possibilities enabled by HoloTPL have greatly demonstrated a noticeable increase in throughput, with the reduction in writing time for periodic structures being typically one or two orders of magnitude, thanks to the ability to generate dozens of foci to be scanned all at once.

Nevertheless, even in the highest performance implementation, TPL still remains behind the possibilities offered by other, more mature micro- and nano-fabrication techniques. Industrial applications require large-scale serial production of 2D microstructures repeated tens of thousands of times, with the surface area of Silicon wafers ranging from 2 up to tens of inches. In this framework, techniques such as mask-exposure UV Lithography, Nanoimprinting, or Roll-to-roll are perhaps less performant in terms of maximum achievable resolution (as seen in Section 2) but ensure higher reliability. Even the microchip manufacturing industry, which is proceeding in broad strides toward reaching the limits set by Moore’s Law, seems to consider techniques such as Extreme UV (EUV) lithography<sup>[245]</sup> the favored choice, as it promises feature sizes on the order of 10 nm or less, making it possible to outperform 7 nm processes, despite the very high costs of instrumentation and facilities.<sup>[246]</sup>

Nevertheless, TPL, and thus HoloTPL, has the advantage of being able to directly process different types of materials, including biocompatible materials, hydrogels, dielectrics, or

even metals, through inclusion of conductive nanoparticles in the resists or photoreduction processes. This makes such techniques particularly attractive for applications such as microfluidics or cell biology. HoloTPL, for example, has shown high potential in a type of application that is severely limiting to competing techniques, namely that of 3D fabrication, allowing for rapid prototyping of a variety of cell filters, microtraps, microcages, or microrobots for drug delivery and microcargos. In this context, Focal Field Engineering (FFE) techniques allow a marked reduction in fabrication time for these types of structures, due to the possibility of polymerizing entire 3D geometries with a single exposure. Moreover, the transition from 2D to 3D fabrication is one of the main perspectives and challenges that the microchip industry is set to face in the coming years.<sup>[247]</sup> There is probably still a long way to go for large-scale adoption of the methods reviewed in this paper, but the intense research and a whole series of brilliant applications proposed in recent years open a real glimmer toward a future in which more and more facilities and technology-driven labs will adopt these promising techniques.

## Acknowledgements

A.B. and M.B. contributed equally to this work. A.B., M.B., and F.P. acknowledged funding from the European Research Council under the European Union’s Horizon 2020 research and innovation program (#677683); M.D.V. acknowledged funding from the European Research Council under the European Union’s Horizon 2020 research and innovation program (#692943). M.B., M.D.V., and F.P. acknowledged funding from the European Research Council under the European Union’s Horizon 2020 research and innovation program (#966674). M.D.V. and F.P. acknowledged that this project has received funding from the European Union’s Horizon 2020 Research and Innovation Program under Grant Agreement No 101016787. M.D.V. was funded by the US National Institutes of Health (U01NS094190). F.P. and M.D.V. were funded by the US National Institutes of Health (1UF1NS108177-01). A.B., F.P., and M.D.V. acknowledge funding from the European Union’s Horizon 2020 research and innovation program under grant agreement (#828972).

## Conflict of Interest

The authors declare no conflict of interest.

## Keywords

computer generated holograms, direct laser writing, holography, two-photon lithography, ultrafast lithography

Received: October 11, 2022  
Revised: November 28, 2022  
Published online: February 22, 2023

- [1] M. Göppert-Mayer, *Ann. Phys.* **1931**, 401, 273.
- [2] W. Kaiser, C. G. B. Garrett, *Phys. Rev. Lett.* **1961**, 7, 229.
- [3] Y. H. Pao, P. M. Rentzepis, *Appl. Phys. Lett.* **2004**, 6, 93.
- [4] D. Bratton, D. Yang, J. Dai, C. K. Ober, *Polym. Adv. Technol.* **2006**, 17, 94.

- [5] V. Harinarayana, Y. C. Shin, *Opt. Laser Technol.* **2021**, *142*, 107180.
- [6] O. Nakamura, S. Kawata, S. Maruo, *Opt. Lett.* **1997**, *22*, 889.
- [7] A. Vyatskikh, R. C. Ng, B. Edwards, R. M. Briggs, J. R. Greer, *Nano Lett.* **2020**, *20*, 3513.
- [8] J. Purto, P. Rogin, A. Verch, V. E. Johansen, R. Hensel, *Nanomaterials* **2019**, *9*, 1495.
- [9] S. Dehaeck, B. Scheid, P. Lambert, in *3D Printed Optics and Additive Photonic Manufacturing, 106750B*, SPIE, Bellingham, WA **2018**.
- [10] O. Vanderpoorten, Q. Peter, P. K. Challa, U. F. Keyser, J. Baumberg, C. F. Kaminski, T. P. J. Knowles, *Microsyst. Nanoeng.* **2019**, *5*, 40.
- [11] J. Song, C. Michas, C. S. Chen, A. E. White, M. W. Grinstaff, *Adv. Healthcare Mater.* **2020**, *9*, 1901217.
- [12] A. Marino, J. Barsotti, G. De Vito, C. Filippeschi, B. Mazzolai, V. Piazza, M. Labardi, V. Mattoli, G. Ciofani, *ACS Appl. Mater. Interfaces* **2015**, *7*, 25574.
- [13] A. Marino, O. Tricinci, M. Battaglini, C. Filippeschi, V. Mattoli, E. Sinibaldi, G. Ciofani, *Small* **2018**, *14*, 1702959.
- [14] B. Spagnolo, A. Balena, R. T. Peixoto, M. Pisanello, L. Sileo, M. Bianco, A. Rizzo, F. Pisano, A. Quattieri, D. D. Lofrumento, F. de Nuccio, J. A. Assad, B. L. Sabatini, M. de Vittorio, F. Pisanello, *Nat. Mater.* **2022**, *21*, 826.
- [15] L. Zheng, K. Kurselis, A. El-Tamer, U. Hinze, C. Reinhardt, L. Overmeyer, B. Chichkov, *Nanoscale Res. Lett.* **2019**, *14*, 134.
- [16] S. Li, C. Lu, X. Wan, S. Zhang, J. Li, Z. He, L. Zhang, *Mater. Today Commun.* **2020**, *24*, 101219.
- [17] S. Zhang, S. Li, X. Wan, J. Ma, N. Li, J. Li, Q. Yin, *Addit. Manuf.* **2021**, *47*, 102358.
- [18] C. Liao, A. Wuethrich, M. Trau, *Appl. Mater. Today* **2020**, *19*, 100635.
- [19] C. M. Spadaccini, in *Three-Dimensional Microfabrication Using Two-Photon Polymerization*, Elsevier, New York **2020**.
- [20] C. Xu, W. W. Webb, in *Topics in Fluorescence Spectroscopy*, Springer US, Boston, MA **2002**.
- [21] C. Cohen-Tannoudji, D. Guéry-Odelin, *Advances in Atomic Physics: An Overview*, World Scientific, Singapore **2011**.
- [22] W. Sibbett, A. A. Lagatsky, C. T. A. Brown, *Opt. Express* **2012**, *20*, 6989.
- [23] V. P. Rajamanickam, L. Ferrara, A. Toma, R. Proietti Zaccaria, G. Das, E. Di Fabrizio, C. Liberale, *Microelectron. Eng.* **2014**, *121*, 135.
- [24] M. Bianco, M. Pisanello, A. Balena, C. Montinaro, F. Pisano, B. Spagnolo, B. L. Sabatini, M. de Vittorio, F. Pisanello, *APL Photonics* **2022**, *7*, 026106.
- [25] T. Zhang, O. Hernandez, R. Chrapkiewicz, A. Shai, M. J. Wagner, Y. Zhang, C.-H. Wu, J. Z. Li, M. Inoue, Y. Gong, B. Ahanonu, H. Zeng, H. Bito, M. J. Schnitzer, *Nat. Methods* **2019**, *16*, 1119.
- [26] A. Balena, M. Bianco, F. Pisano, M. Pisanello, L. Sileo, B. L. Sabatini, M. de Vittorio, F. Pisanello, *Opt. Express* **2020**, *28*, 21368.
- [27] W.-E. Lu, Y.-L. Zhang, M.-L. Zheng, Y.-P. Jia, J. Liu, X.-Z. Dong, Z.-S. Zhao, C.-B. Li, Y. Xia, T.-C. Ye, X.-M. Duan, *Opt. Mater. Express* **2013**, *3*, 1660.
- [28] J. T. Fourkas, in *Three-Dimensional Microfabrication Using Two-photon Polymerization*, Elsevier, New York **2016**.
- [29] S. Heiskanen, Z. Geng, J. Mastomäki, I. J. Maasilta, *Adv. Eng. Mater.* **2020**, *22*, 1901290.
- [30] A. Braun, S. A. Maier, *ACS Sens.* **2016**, *1*, 1155.
- [31] G. Moad, D. H. Solomon, *The Chemistry of Radical Polymerization*, Elsevier Science, Oxford **2005**.
- [32] W. H. Koppenol, *Pure Appl. Chem.* **2000**, *72*, 437.
- [33] K.-S. Lee, D.-Y. Yang, S. H. Park, R. H. Kim, *Polym. Adv. Technol.* **2006**, *17*, 72.
- [34] J. Serbin, A. Egbert, A. Ostendorf, B. N. Chichkov, R. Houbertz, G. Domann, J. Schulz, C. Cronauer, L. Fröhlich, M. Popall, *Opt. Lett.* **2003**, *28*, 301.
- [35] D. Jang, L. R. Meza, F. Greer, J. R. Greer, *Nat. Mater.* **2013**, *12*, 893.
- [36] T. Baldacchini, V. Nuñez, C. N. LaFratta, J. S. Grech, V. I. Vullev, R. Zadayan, in *Laser 3D Manufacturing II* (Eds.: H. Helvajian, A. Piqué, M. Wegener, B. Gu), SPIE, Bellingham, WA **2015**.
- [37] Z. Li, N. Pucher, K. Cicha, J. Torgersen, S. C. Ligon, A. Ajami, W. Husinsky, A. Rosspeintner, E. Vauthey, S. Naumov, T. Scherzer, J. Stampfl, R. Liska, *Macromolecules* **2013**, *46*, 352.
- [38] B. E. A. Saleh, M. C. Teich, *Fundamentals of Photonics*, John Wiley & Sons, Inc., New York, USA **1991**.
- [39] V. F. Paz, M. Emons, K. Obata, A. Ovsianikov, S. Peterhänsel, K. Frenner, C. Reinhardt, B. Chichkov, U. Morgner, W. Osten, *J. Laser Appl.* **2012**, *24*, 042004.
- [40] L. Zheng, K. Kurselis, A. El-Tamer, U. Hinze, C. Reinhardt, L. Overmeyer, B. Chichkov, *Nanoscale Res. Lett.* **2019**, *14*, 134.
- [41] L. Li, R. R. Gattass, E. Gershgoren, H. Hwang, J. T. Fourkas, *Science* **2009**, *324*, 910.
- [42] Z. Gan, Y. Cao, R. A. Evans, M. Gu, *Nat. Commun.* **2013**, *4*, 2061.
- [43] N. Vasilantonakis, K. Terzaki, I. Sakellari, V. Puryls, D. Gray, C. M. Soukoulis, M. Vamvakaki, M. Kafesaki, M. Farsari, *Adv. Mater.* **2012**, *24*, 1101.
- [44] C. N. LaFratta, J. T. Fourkas, T. Baldacchini, R. A. Farrer, *Angew. Chem. Int. Ed.* **2007**, *46*, 6238.
- [45] E. Andrzejewska, *Prog. Polym. Sci.* **2001**, *26*, 605.
- [46] H.-B. Sun, K. Takada, M.-S. Kim, K.-S. Lee, S. Kawata, *Appl. Phys. Lett.* **2003**, *83*, 1104.
- [47] K.-S. Lee, R. Kim, P. Prabhakaran, D.-Y. Yang, T. Lim, S. H. Park, *J. Nonlinear Opt. Phys. Mater.* **2007**, *16*, 59.
- [48] R. J. DeVoe, H. W. Kalweit, C. A. Leatherdale, T. R. Williams, in *Multiphoton Absorption and Nonlinear Transmission Processes* (Eds.: K. D. Belfield, S. J. Caracci, F. Kajzar, C. M. Lawson, A. T. Yeates), SPIE, Bellingham, WA **2003**.
- [49] H.-B. Sun, T. Tanaka, S. Kawata, *Appl. Phys. Lett.* **2002**, *80*, 3673.
- [50] H.-B. Sun, M. Maeda, K. Takada, J. W. M. Chon, M. Gu, S. Kawata, *Appl. Phys. Lett.* **2003**, *83*, 819.
- [51] D. Tan, Y. Li, F. Qi, H. Yang, Q. Gong, X. Dong, X. Duan, *Appl. Phys. Lett.* **2007**, *90*, 071106.
- [52] X.-Z. Dong, Z.-S. Zhao, X.-M. Duan, *Appl. Phys. Lett.* **2008**, *92*, 091113.
- [53] J. V. Crivello, E. Reichmanis, *Chem. Mater.* **2014**, *26*, 533.
- [54] X. Zhou, Y. Hou, J. Lin, *AIP Adv.* **2015**, *5*, 030701.
- [55] W.-E. Lu, X.-Z. Dong, W.-Q. Chen, Z.-S. Zhao, X.-M. Duan, *J. Mater. Chem.* **2011**, *21*, 5650.
- [56] K. Takada, H.-B. Sun, S. Kawata, *Appl. Phys. Lett.* **2005**, *86*, 071122.
- [57] S. H. Park, T. W. Lim, D.-Y. Yang, R. H. Kim, K.-S. Lee, *Macromol. Res.* **2006**, *14*, 559.
- [58] T. A. Klar, E. Engel, S. W. Hell, *Phys. Rev. E* **2001**, *64*, 066613.
- [59] H.-B. Sun, S. Kawata, in *NMR • 3D Analysis • Photopolymerization. Advances in Polymer Science*, Springer, Berlin **2006**.
- [60] R. Wollhofen, J. Katzmann, C. Hrelescu, J. Jacak, T. A. Klar, *Opt. Express* **2013**, *21*, 10831.
- [61] J. Fischer, M. Wegener, *Opt. Mater. Express* **2011**, *1*, 614.
- [62] T. F. Scott, B. A. Kowalski, A. C. Sullivan, C. N. Bowman, R. R. McLeod, *Science* **2009**, *324*, 913.
- [63] M. P. Stocker, L. Li, R. R. Gattass, J. T. Fourkas, *Nat. Chem.* **2011**, *3*, 223.
- [64] Y. Cao, Z. Gan, B. Jia, R. A. Evans, M. Gu, *Opt. Express* **2011**, *19*, 19486.
- [65] J. Fischer, M. Wegener, *Laser Photonics Rev.* **2013**, *7*, 22.
- [66] P. Prabhakaran, Commercial Direct Laser Writing (DLW) Machines, **2020**.
- [67] S. M. Kuebler, M. Rumi, in *Encyclopedia of Modern Optics*, Elsevier, Amsterdam **2005**.
- [68] C. R. K. Marrian, D. M. Tennant, *J. Vac. Sci. Technol. A* **2003**, *21*, S207.
- [69] M. Malinauskas, A. Žukauskas, S. Hasegawa, Y. Hayasaki, V. Mizeikis, R. Buividas, S. Juodkazis, *Light Sci. Appl.* **2016**, *5*, 16133.

- [70] M. Malinauskas, M. Farsari, A. Piskarskas, S. Juodkazis, *Phys. Rep.* **2013**, 533, 1.
- [71] C. N. LaFratta, L. Li, in *Three-Dimensional Microfabrication Using Two-Photon Polymerization*, 2nd ed., Elsevier, New York **2020**.
- [72] B. Jaeggi, B. Neuenschwander, M. Zimmermann, M. Zecherle, E. W. Boeckler, in *Laser Applications in Microelectronic and Optoelectronic Manufacturing (LAMOM) XXI* (Eds.: B. Neuenschwander, S. Roth, C. P. Grigoropoulos, T. Makimura), SPIE, Bellingham, WA **2016**.
- [73] N. GmbH, Photonic Professional GT2, **2022**.
- [74] J. S. Oakdale, R. F. Smith, J. Forien, W. L. Smith, S. J. Ali, L. B. Bayu Aji, T. M. Willey, J. Ye, A. W. van Buuren, M. A. Worthington, S. T. Prisbrey, H. Park, P. A. Amendt, T. F. Baumann, J. Biener, *Adv. Funct. Mater.* **2017**, 27, 1702425.
- [75] Q. Zhan, in *Three-Dimensional Microfabrication Using Two-photon Polymerization* (Ed.: T. Baldacchini), William Andrew Publishing, Oxford **2016**.
- [76] T. W. Lim, S. H. Park, D.-Y. Yang, *Microelectron. Eng.* **2005**, 77, 382.
- [77] M. Malinauskas, V. Purlys, M. Rutkauskas, R. Gadonas, in *Micromachining and Microfabrication Process Technology XIV* (Eds.: M.-A. Maher, J.-C. Chiao, P. J. Resnick), SPIE, Bellingham, WA **2009**.
- [78] M. Pisanello, D. Zheng, A. Balena, F. Pisano, M. De Vittorio, F. Pisanello, *PLoS One* **2022**, 17, 0265678.
- [79] G. Kumi, C. O. Yanez, K. D. Belfield, J. T. Fourkas, *Lab Chip* **2010**, 10, 1057.
- [80] L. Jonušauskas, D. Gailevičius, S. Rekštytė, T. Baldacchini, S. Juodkazis, M. Malinauskas, *Opt. Express* **2019**, 27, 15205.
- [81] M. Rybin, I. Shishkin, K. Samusev, P. Belov, Y. Kivshar, R. Kiyon, B. Chichkov, M. Limonov, *Crystals* **2015**, 5, 61.
- [82] I. I. Shishkin, M. V. Rybin, K. B. Samusev, M. F. Limonov, R. V. Kiyon, B. N. Chichkov, Y. S. Kivshar, P. A. Belov, *JETP Lett.* **2014**, 99, 531.
- [83] M. Carlotti, V. Mattoli, *Small* **2019**, 15, 1902687.
- [84] S. Kawata, H.-B. Sun, T. Tanaka, K. Takada, *Nature* **2001**, 412, 697.
- [85] M. Farsari, G. Filippidis, K. Sambani, T. S. Drakakis, C. Fotakis, *J. Photochem. Photobiol. A* **2006**, 181, 132.
- [86] E. D. Lemma, F. Rizzi, T. Dattoma, B. Spagnolo, L. Sileo, A. Quattieri, M. De Vittorio, F. Pisanello, *IEEE Trans. Nanotechnol.* **2016**, 16, 23.
- [87] H. E. Williams, D. J. Freppon, S. M. Kuebler, R. C. Rumpf, M. A. Melino, *Opt. Express* **2011**, 19, 22910.
- [88] T. Baldacchini, C. N. LaFratta, R. A. Farrer, M. C. Teich, B. E. A. Saleh, M. J. Naughton, J. T. Fourkas, *J. Appl. Phys.* **2004**, 95, 6072.
- [89] G. Panusa, Y. Pu, J. Wang, C. Moser, D. Psaltis, *Polymers* **2020**, 12, 2485.
- [90] C. A. Coenjarts, C. K. Ober, *Chem. Mater.* **2004**, 16, 5556.
- [91] A. Ovsianikov, B. Chichkov, P. Mente, N. A. Monteiro-Riviere, A. Doraiswamy, R. J. Narayan, *Int. J. Appl. Ceram. Technol.* **2007**, 4, 22.
- [92] J. C. Sanger, B. R. Pauw, H. Sturm, J. Gunster, *Open Ceramics* **2020**, 4, 100040.
- [93] T. Zandrini, N. Liaros, L. J. Jiang, Y. F. Lu, J. T. Fourkas, R. Osellame, T. Baldacchini, *Opt. Mater. Express* **2019**, 9, 2601.
- [94] Y. Li, S. Park, M. McLamb, M. Lata, S. Schochle, D. Childers, I. D. Aggarwal, M. K. Poutous, G. Boreman, T. Hofmann, *Opt. Mater. Express* **2019**, 9, 4318.
- [95] J. B. Mueller, J. Fischer, F. Mayer, M. Kadlic, M. Wegener, *Adv. Mater.* **2014**, 26, 6566.
- [96] B. H. Cumpston, S. P. Ananthavel, S. Barlow, D. L. Dyer, J. E. Ehrlich, L. L. Erskine, A. A. Heikal, S. M. Kuebler, I.-Y. S. Lee, D. McCord-Maughan, J. Qin, H. Rockel, M. Rumi, X.-L. Wu, S. R. Marder, J. W. Perry, *Nature* **1999**, 398, 51.
- [97] J.-F. Xing, X.-Z. Dong, W.-Q. Chen, X.-M. Duan, N. Takeyasu, T. Tanaka, S. Kawata, *Appl. Phys. Lett.* **2007**, 90, 131106.
- [98] P. Kiefer, V. Hahn, M. Nardi, L. Yang, E. Blasco, C. Barner-Kowollik, M. Wegener, *Adv. Opt. Mater.* **2020**, 8, 2000895.
- [99] S. M. Kuebler, M. Rumi, T. Watanabe, K. Braun, B. H. Cumpston, A. A. Heikal, L. L. Erskine, S. Thayumanavan, S. Barlow, S. R. Marder, J. W. Perry, *J. Photopolym. Sci. Technol.* **2001**, 14, 657.
- [100] Y.-C. Zheng, Y.-Y. Zhao, M.-L. Zheng, S.-L. Chen, J. Liu, F. Jin, X.-Z. Dong, Z.-S. Zhao, X.-M. Duan, *ACS Appl. Mater. Interfaces* **2019**, 11, 1782.
- [101] W. Gao, H. Chao, Y.-C. Zheng, W.-C. Zhang, J. Liu, F. Jin, X.-Z. Dong, Y.-H. Liu, S.-J. Li, M.-L. Zheng, *ACS Appl. Mater. Interfaces* **2021**, 13, 27796.
- [102] N. Uppal, *J. Micro/Nanolithogr. MEMS, MOEMS* **2008**, 7, 043002.
- [103] T. Baldacchini, S. Snider, R. Zadayan, *Opt. Express* **2012**, 20, 29890.
- [104] M. Malinauskas, P. Danilevičius, S. Juodkazis, *Opt. Express* **2011**, 19, 5602.
- [105] M. Malinauskas, A. Žukauskas, G. Bičkauskaitė, R. Gadonas, S. Juodkazis, *Opt. Express* **2010**, 18, 10209.
- [106] A. K. Nguyen, R. J. Narayan, *Mater. Today* **2017**, 20, 314.
- [107] J. Fischer, J. B. Mueller, J. Kaschke, T. J. A. Wolf, A.-N. Unterreiner, M. Wegener, *Opt. Express* **2013**, 21, 26244.
- [108] J. B. Mueller, J. Fischer, Y. J. Mange, T. Nann, M. Wegener, *Appl. Phys. Lett.* **2013**, 103, 123107.
- [109] D. Perevozniak, R. Nazir, R. Kiyon, K. Kurselis, B. Koszarna, D. T. Gryko, B. N. Chichkov, *Opt. Express* **2019**, 27, 25119.
- [110] F. Formanek, N. Takeyasu, T. Tanaka, K. Chiyoda, A. Ishikawa, S. Kawata, *Opt. Express* **2006**, 14, 800.
- [111] F. Formanek, N. Takeyasu, T. Tanaka, K. Chiyoda, A. Ishikawa, S. Kawata, *Appl. Phys. Lett.* **2006**, 88, 083110.
- [112] G. Mallory, J. B. Hajdu, *Electroless Plating: Fundamentals and Applications*, American Electroplaters and Surface Finishers Society, Orlando **1990**.
- [113] J. Kato, N. Takeyasu, Y. Adachi, H.-B. Sun, S. Kawata, *Appl. Phys. Lett.* **2005**, 86, 044102.
- [114] R. Guo, S. Xiao, X. Zhai, J. Li, A. Xia, W. Huang, *Opt. Express* **2006**, 14, 810.
- [115] T.-T. Chung, Y.-T. Tu, Y.-H. Hsueh, S.-Y. Chen, W.-J. Li, *Int. J. Autom. Smart Technol.* **2013**, 3, 131.
- [116] Z. He, Y.-H. Lee, D. Chanda, S.-T. Wu, *Opt. Express* **2018**, 26, 21184.
- [117] A. Antonini, A. Sattin, M. Moroni, S. Bovetti, C. Moretti, F. Succol, A. Forli, D. Vecchia, V. P. Rajamanickam, A. Bertoncini, S. Panzeri, C. Liberale, T. Fellin, *Elife* **2020**, 9, 58882.
- [118] B. Kaehr, J. B. Shear, *J. Am. Chem. Soc.* **2007**, 129, 1904.
- [119] D. Kim, P. T. C. So, *Opt. Lett.* **2010**, 35, 1602.
- [120] E. T. Ritschdorff, R. Nielson, J. B. Shear, *Lab Chip* **2012**, 12, 867.
- [121] W. Chu, Y. Tan, P. Wang, J. Xu, W. Li, J. Qi, Y. Cheng, *Adv. Mater. Technol.* **2018**, 3, 1700396.
- [122] D. Oron, E. Tal, Y. Silberberg, *Opt. Express* **2005**, 13, 1468.
- [123] R. Nielson, B. Kaehr, J. B. Shear, *Small* **2009**, 5, 120.
- [124] Y.-H. Liu, Y.-Y. Zhao, F. Jin, X.-Z. Dong, M.-L. Zheng, Z.-S. Zhao, X.-M. Duan, *Nano Lett.* **2021**, 21, 3915.
- [125] T.-W. Wang, X.-Z. Dong, F. Jin, Y.-Y. Zhao, X.-Y. Liu, M.-L. Zheng, X.-M. Duan, *Opt. Express* **2022**, 30, 36791.
- [126] S. K. Saha, D. Wang, V. H. Nguyen, Y. Chang, J. S. Oakdale, S.-C. Chen, *Science* **2019**, 366, 105.
- [127] J.-H. Jang, D. Dendukuri, T. A. Hatton, E. L. Thomas, P. S. Doyle, *Angew. Chem. Int. Ed.* **2007**, 46, 9027.
- [128] H. Jee, M.-J. Park, K. Jeon, C. Jeong, J. Lee, *Appl. Sci.* **2021**, 11, 6559.
- [129] A. Biswas, I. S. Bayer, A. S. Biris, T. Wang, E. Dervishi, F. Faupel, *Adv. Colloid Interface Sci.* **2012**, 170, 2.
- [130] S. M. Kirkpatrick, J. W. Baur, C. M. Clark, L. R. Denny, D. W. Tomlin, B. R. Reinhardt, R. Kannan, M. O. Stone, *Appl. Phys. A* **1999**, 69, 461.
- [131] M. Campbell, D. N. Sharp, M. T. Harrison, R. G. Denning, A. J. Turberfield, *Nature* **2000**, 404, 53.

- [132] T. Kondo, S. Matsuo, S. Juodkazis, V. Mizeikis, H. Misawa, *Appl. Phys. Lett.* **2003**, *82*, 2758.
- [133] C. Maibohm, O. F. Silvestre, J. Borme, M. Sinou, K. Heggarty, J. B. Nieder, *Sci. Rep.* **2020**, *10*, 8740.
- [134] S. Jeon, J.-U. Park, R. Cirelli, S. Yang, C. E. Heitzman, P. V. Braun, P. J. A. Kenis, J. A. Rogers, *Proc. Natl. Acad. Sci. USA* **2004**, *101*, 12428.
- [135] J. W. Rinne, S. Gupta, P. Wiltzius, *Opt. Express* **2008**, *16*, 663.
- [136] S. Jeon, Y.-S. Nam, D. J.-L. Shir, J. A. Rogers, A. Hamza, *Appl. Phys. Lett.* **2006**, *89*, 253101.
- [137] S. Jeon, E. Menard, J.-U. Park, J. Maria, M. Meitl, J. Zaumseil, J. A. Rogers, *Adv. Mater.* **2004**, *16*, 1369.
- [138] M. Malinauskas, A. Žukauskas, V. Purlys, K. Belazaras, A. Momot, D. Paipulas, R. Gadonas, A. Piskarskas, H. Gilbergs, A. Gaidukevičiūtė, I. Sakellari, M. Farsari, S. Juodkazis, *J. Opt.* **2010**, *12*, 124010.
- [139] J. Whitfield, *Nature* **2001**, *414*, 578.
- [140] Y. Xia, G. M. Whitesides, *Angew. Chem. Int. Ed.* **1998**, *37*, 550.
- [141] C. N. LaFratta, T. Baldacchini, R. A. Farrer, J. T. Fourkas, M. C. Teich, B. E. A. Saleh, M. J. Naughton, *J. Phys. Chem. B* **2004**, *108*, 11256.
- [142] I. Miranda, A. Souza, P. Sousa, J. Ribeiro, E. M. S. Castanheira, R. Lima, G. Minas, *J. Funct. Biomater.* **2021**, *13*, 2.
- [143] C. N. LaFratta, L. Li, J. T. Fourkas, *Proc. Natl. Acad. Sci. USA* **2006**, *103*, 8589.
- [144] T. W. Lim, S. H. Park, D.-Y. Yang, T. A. Pham, D. H. Lee, D.-P. Kim, S.-I. Chang, J.-B. Yoon, *Microelectron. Eng.* **2006**, *83*, 2475.
- [145] Y. Daicho, T. Murakami, T. Hagiwara, S. Maruo, *Opt. Mater. Express* **2013**, *3*, 875.
- [146] D. Gabor, *Nature* **1948**, *161*, 777.
- [147] S. Davies, Y. Hu, N. Jiang, J. Blyth, M. Kaminska, Y. Liu, A. K. Yetisen, *Adv. Funct. Mater.* **2021**, *31*, 2105645.
- [148] W. Yang, R. Yuste, *Curr. Opin. Neurobiol.* **2018**, *50*, 211.
- [149] H. Adesnik, L. Abdeladim, *Nat. Neurosci.* **2021**, *24*, 1356.
- [150] Y. Du, S. Turtaev, I. T. Leite, A. Lorenz, J. Kobelke, K. Wondraczek, T. Čížmár, *Light* **2022**, *3*, 408.
- [151] L. Huang, S. Zhang, T. Zentgraf, *Nanophotonics* **2018**, *7*, 1169.
- [152] G. Jin, L. Cao, Q. Jiang, *Adv. Opt. Photonics* **2019**, *11*, 518.
- [153] X. Lin, J. Liu, J. Hao, K. Wang, Y. Zhang, H. Li, H. Horimai, X. Tan, *Opto-Electron. Adv.* **2020**, *3*, 190004.
- [154] P. Hariharan, *Optical Holography*, Cambridge University Press, Cambridge **1996**.
- [155] E. N. Leith, J. Upatnieks, *J. Opt. Soc. Am.* **1962**, *52*, 1123.
- [156] E. N. Leith, J. Upatnieks, *J. Opt. Soc. Am.* **1963**, *53*, 1377.
- [157] E. N. Leith, J. Upatnieks, *J. Opt. Soc. Am.* **1964**, *54*, 1295.
- [158] G. W. Stroke, *Appl. Phys. Lett.* **1965**, *6*, 201.
- [159] G. W. Stroke, D. Brumm, A. Funkhouser, *J. Opt. Soc. Am.* **1965**, *55*, 1327.
- [160] A. vander Lugt, *IEEE Trans. Inf. Theory* **1964**, *10*, 139.
- [161] B. R. Brown, A. W. Lohmann, *Appl. Opt.* **1966**, *5*, 967.
- [162] G. Tricoles, *Appl. Opt.* **1987**, *26*, 4351.
- [163] W. J. Dallas, in *Digital Holography and Three-Dimensional Display: Principles and Applications* (Ed.: T.-C. Poon), Springer US, Boston, MA **2006**, p. 1.
- [164] R. W. Gerchberg, W. O. Saxton, *Optik* **1972**, *35*, 237.
- [165] A. S. Mikryukov, I. V. Il'ina, T. Yu. Cherezova, *Atmos. Oceanic Opt.* **2010**, *23*, 229.
- [166] W. Wan, J. Gao, X. Yang, *Adv. Opt. Mater.* **2017**, *5*, 1700541.
- [167] C. Guo, C. Wei, J. Tan, K. Chen, S. Liu, Q. Wu, Z. Liu, *Opt. Lasers Eng.* **2017**, *89*, 2.
- [168] H. Kim, M. Kim, W. Lee, J. Ahn, *Opt. Express* **2019**, *27*, 2184.
- [169] A. Atajanov, A. Zhanov, S. Yang, *Nano* **2018**, *6*, 2.
- [170] D. Delahaye, S. Chaimatanan, M. Mongeau, in *Handbook of Metaheuristics* (Eds.: M. Gendreau, J.-Y. Potvin), Springer, New York LLC **2019**.
- [171] A. Robel, *IEEE Trans. Audio Speech Lang. Process.* **2006**, *14*, 1440.
- [172] E. R. Dufresne, G. C. Spalding, M. T. Dearing, S. A. Sheets, D. G. Grier, *Rev. Sci. Instrum.* **2001**, *72*, 1810.
- [173] M. Pasienski, B. Demarco, M. Krämer, D. Z. Anderson, M. J. Holland, *Opt. Express* **2008**, *16*, 2176.
- [174] C. Zhang, Y. Hu, W. Du, P. Wu, S. Rao, Z. Cai, Z. Lao, B. Xu, J. Ni, J. Li, G. Zhao, D. Wu, J. Chu, K. Sugioka, *Sci. Rep.* **2016**, *6*, 33281.
- [175] J. Bengtsson, *Appl. Opt.* **1994**, *33*, 6879.
- [176] M. Sakakura, T. Sawano, Y. Shimotsuma, K. Miura, K. Hiraio, D. B. Keck, A. J. Morrow, D. A. Nolan, D. A. Thompson, M. H. Hu, J. Z. Huang, R. Scarmozzino, M. Levy, R. M. Osgood, *Opt. Express* **2010**, *18*, 12136.
- [177] S. Turtaev, I. T. Leite, K. J. Mitchell, M. J. Padgett, D. B. Phillips, T. Čížmár, *Opt. Express* **2017**, *25*, 29874.
- [178] D. Engström, M. Persson, M. Goksör, *Opt. Express* **2012**, *20*, 7741.
- [179] Ibsen Photonics, DMD Spectrometers, <https://www.ibsen.com/resources/spectrometer-resources/dmd-spectrometers/> (accessed: July 2022).
- [180] Hamamatsu, Phase spatial light modulator LCOS-SLM, [https://www.hamamatsu.com/resources/pdf/ssd/e12\\_handbook\\_lcos\\_slm.pdf](https://www.hamamatsu.com/resources/pdf/ssd/e12_handbook_lcos_slm.pdf) (accessed: January 2022).
- [181] N. J. Sofroniew, D. Flickinger, J. King, K. Svoboda, *Elife* **2016**, *5*, 14472.
- [182] E. D. Lemma, F. Rizzi, T. Dattoma, B. Spagnolo, L. Sileo, A. Qualtieri, M. de Vittorio, F. Pisanello, *IEEE Trans. Nanotechnol.* **2016**, *16*, 23.
- [183] N. Matsumoto, H. Itoh, T. Inoue, T. Otsu, H. Toyoda, H. Lin, J. Qu, X. Peng, H. Niu, B. Z. Gao, *Opt. Express* **2014**, *22*, 24722.
- [184] A. Takita, H. Takahashi, S. Hasegawa, Y. Hayasaki, *Opt. Express* **2008**, *16*, 16592.
- [185] S. D. Gittard, A. Nguyen, K. Obata, A. Koroleva, R. J. Narayan, B. N. Chichkov, *Biomed. Opt. Express* **2011**, *2*, 3167.
- [186] L. Yang, A. El-Tamer, U. Hinze, J. Li, Y. Hu, W. Huang, J. Chu, B. N. Chichkov, *Opt. Lasers Eng.* **2015**, *70*, 26.
- [187] S. Hasegawa, H. Ito, H. Toyoda, Y. Hayasaki, *Opt. Express* **2016**, *24*, 18513.
- [188] K. Obata, J. Koch, U. Hinze, B. N. Chichkov, *Opt. Express* **2010**, *18*, 17193.
- [189] E. T. Ritschdorff, R. Nielson, J. B. Shear, *Lab Chip* **2012**, *12*, 867.
- [190] Q. Geng, D. Wang, P. Chen, S. C. Chen, *Nat. Commun.* **2019**, *10*, 2179.
- [191] D. G. Papazoglou, M. Farsari, M. Manousidaki, S. Tzortzakos, *Opt. Lett.* **2020**, *45*, 85.
- [192] G. Vizsnyczai, L. Kelemen, P. Ormos, *Opt. Express* **2014**, *22*, 24217.
- [193] L. Yang, J. Li, Y. Hu, C. Zhang, Z. Lao, W. Huang, J. Chu, *Opt. Commun.* **2014**, *331*, 82.
- [194] C. Zhang, Y. Hu, J. Li, Z. Lao, J. Ni, J. Chu, W. Huang, D. Wu, *Appl. Phys. Lett.* **2014**, *105*, 221104.
- [195] C. Zhang, Y. Hu, J. Li, G. Li, J. Chu, W. Huang, E. J. Smith, S. Schulze, S. Kiravittaya, Y. Mei, S. Sanchez, O. G. Schmidt, G. Huang, D. J. Thurmer, E. Coric, *Opt. Express* **2014**, *22*, 3983.
- [196] C. Zhang, Y. Hu, J. Li, Z. Lao, B. Xu, J. Ni, Z. Cai, D. Wu, J. Chu, *Opt. Eng.* **2016**, *55*, 035102.
- [197] D. McGloin, K. Dholakia, *Contemp. Phys.* **2005**, *46*, 15.
- [198] N. Chattrapiban, E. A. Rogers, D. Cofield, I. W. T. Hill, R. Roy, *Opt. Lett.* **2003**, *28*, 2183.
- [199] B. Liu, D. Wu, G. Zhao, H. Jiang, J. Chu, J. Li, K. Xie, L. Yang, S. Ji, S. Liu, W. Huang, W. Du, Y. Hu, *Opt. Express* **2017**, *25*, 8144.
- [200] M. Manousidaki, D. G. Papazoglou, M. Farsari, S. Tzortzakos, *Opt. Mater. Express* **2019**, *9*, 2838.
- [201] L. Yang, A. El-Tamer, U. Hinze, J. Li, Y. Hu, W. Huang, J. Chu, B. N. Chichkov, *Appl. Phys. Lett.* **2014**, *105*, 041110.
- [202] L. Yang, D. Qian, C. Xin, Z. Hu, S. Ji, D. Wu, Y. Hu, J. Li, W. Huang, J. Chu, *Opt. Lett.* **2017**, *42*, 743.
- [203] L. Yang, D. Qian, C. Xin, Z. Hu, S. Ji, D. Wu, Y. Hu, J. Li, W. Huang, J. Chu, *Appl. Phys. Lett.* **2017**, *110*, 221103.
- [204] S.-J. Zhang, Y. Li, Z.-P. Liu, J.-L. Ren, Y.-F. Xiao, H. Yang, Q. Gong, *Appl. Phys. Lett.* **2014**, *105*, 061101.

- [205] J. Ni, J. Ni, Y. Hu, Y. Hu, S. Liu, Z. Lao, S. Ji, D. Pan, C. Zhang, B. Xu, J. Li, D. Wu, J. Chu, *Opt. Lett.* **2021**, *46*, 1401.
- [206] J. Ni, C. Wang, C. Zhang, Y. Hu, L. Yang, Z. Lao, B. Xu, J. Li, D. Wu, J. Chu, *Light Sci Appl* **2017**, *6*, 17011.
- [207] D. Yang, L. Liu, Q. Gong, Y. Li, *Macromol. Rapid Commun.* **2019**, *40*, 1900041.
- [208] B. Luther-Davis, B. P. Cumming, M. Gu, S. Debbarma, *Opt. Express* **2013**, *21*, 19135.
- [209] H. E. Williams, Z. Luo, S. M. Kuebler, *Opt. Express* **2012**, *20*, 25030.
- [210] B. Horváth, P. Ormos, L. Kelemen, *Micromachines* **2017**, *8*, 219.
- [211] E. H. Waller, G. von Freymann, A. H. Buist, M. Müller, J. Squier, G. J. Brakenhoff, *Opt. Express* **2013**, *21*, 21708.
- [212] A. Jesacher, M. J. Booth, *Opt. Express* **2010**, *18*, 21090.
- [213] E. H. Waller, G. von Freymann, M. Renner, *Opt. Express* **2012**, *20*, 24949.
- [214] L. Kelemen, P. Ormos, G. Vizsnyiczai, *J. Eur. Opt. Soc. Rapid Publ.* **2011**, *6*, 11029.
- [215] S. Hasegawa, Y. Hayasaki, *Opt. Lett.* **2014**, *39*, 478.
- [216] M. Ren, W. Lu, Q. Shao, F. Han, W. Ouyang, T. Zhang, C. C. L. Wang, S.-C. Chen, *Opt. Express* **2021**, *29*, 44250.
- [217] P. S. Salter, M. J. Booth, *Light: Sci. Appl.* **2019**, *8*, 110.
- [218] G. M. Whitesides, *Nature* **2006**, *442*, 368.
- [219] C. Zhang, H. Ye, R. Cao, S. Ji, H. Zhang, L. Zhao, S. Wu, H. Zhai, *Chin. Opt. Lett.* **2022**, *20*, 023801.
- [220] B. Xu, Y. Shi, Z. Lao, J. Ni, G. Li, Y. Hu, J. Li, J. Chu, D. Wu, K. Sugioka, *Lab Chip* **2018**, *18*, 442.
- [221] B. Xu, W.-Q. Du, J.-W. Li, Y.-L. Hu, L. Yang, C.-C. Zhang, G.-Q. Li, Z.-X. Lao, J.-C. Ni, J.-R. Chu, D. Wu, S.-L. Liu, K. Sugioka, *Sci. Rep.* **2016**, *6*, 19989.
- [222] B. Xu, W. Hu, W. Du, Y. Hu, C. Zhang, Z. Lao, J. Ni, J. Li, D. Wu, J. Chu, K. Sugioka, *Opt. Express* **2017**, *25*, 16739.
- [223] K. Hu, L. Yang, D. Jin, J. Li, S. Ji, C. Xin, Y. Hu, D. Wu, L. Zhang, J. Chu, *Lab Chip* **2019**, *19*, 3988.
- [224] C. Zhang, J. Zhang, R. Chen, J. Li, C. Wang, R. Cao, J. Zhang, H. Ye, H. Zhai, K. Sugioka, *Opt. Lett.* **2020**, *45*, 3929.
- [225] B. Xu, S. Ji, D. Pan, W. Hu, S. Zhu, Y. Hu, J. Li, D. Wu, J. Chu, K. Sugioka, *Opt. Lett.* **2020**, *45*, 1071.
- [226] S. Ji, R. Li, Z. Cai, D. Pan, L. Yang, Y. Hu, J. Li, D. Wu, J. Chu, *Opt. Lett.* **2019**, *44*, 5073.
- [227] E. D. Lemma, B. Spagnolo, M. de Vittorio, F. Pisanello, *Trends Biotechnol.* **2019**, *37*, 358.
- [228] E. D. Lemma, S. Sergio, B. Spagnolo, M. Pisanello, L. Algieri, M. A. Coluccia, M. Maffia, M. de Vittorio, F. Pisanello, *Microelectron. Eng.* **2018**, *190*, 11.
- [229] T. Zandrini, O. Shan, V. Parodi, G. Cerullo, M. T. Raimondi, R. Osellame, *Sci. Rep.* **2019**, *9*, 11761.
- [230] L. Zhang, B. Liu, C. Wang, C. Xin, R. Li, D. Wang, L. Xu, S. Fan, J. Zhang, C. Zhang, Y. Hu, J. Li, D. Wu, L. Zhang, J. Chu, *Nano Lett.* **2022**, *22*, 5277.
- [231] S. Ji, L. Yang, Y. Hu, J. Ni, W. Du, J. Li, G. Zhao, D. Wu, J. Chu, *Small* **2017**, *13*, 1701190.
- [232] D. Pan, Z. Cai, S. Ji, S. Fan, P. Wang, Z. Lao, L. Yang, J. Ni, C. Wang, J. Li, Y. Hu, D. Wu, S. Chen, J. Chu, *ACS Appl. Mater. Interfaces* **2018**, *10*, 36369.
- [233] C. Wang, L. Yang, Y. Hu, S. Rao, Y. Wang, D. Pan, S. Ji, C. Zhang, Y. Su, W. Zhu, J. Li, D. Wu, J. Chu, *ACS Nano* **2019**, *13*, 4667.
- [234] Z. Lao, N. Xia, S. Wang, T. Xu, X. Wu, L. Zhang, *Micromachines* **2021**, *12*, 465.
- [235] R. Li, D. Jin, D. Pan, S. Ji, C. Xin, G. Liu, S. Fan, H. Wu, J. Li, Y. Hu, D. Wu, L. Zhang, J. Chu, *ACS Nano* **2020**, *14*, 5233.
- [236] S. Ji, L. Yang, C. Zhang, Z. Cai, Y. Hu, J. Li, D. Wu, J. Chu, *Opt. Lett.* **2018**, *43*, 3514.
- [237] C. Xin, L. Yang, J. Li, Y. Hu, D. Qian, S. Fan, K. Hu, Z. Cai, H. Wu, D. Wang, D. Wu, J. Chu, *Adv. Mater.* **2019**, *31*, 1808226.
- [238] L. Yang, X. Chen, L. Wang, Z. Hu, C. Xin, M. Hippler, W. Zhu, Y. Hu, J. Li, Y. Wang, L. Zhang, D. Wu, J. Chu, *Adv. Funct. Mater.* **2019**, *29*, 1905745.
- [239] C. Xin, D. Jin, R. Li, D. Wang, Z. Ren, B. Liu, C. Chen, L. Li, S. Liu, B. Xu, Y. Zhang, Y. Hu, J. Li, L. Zhang, D. Wu, J. Chu, *Small* **2022**, *18*, 2202272.
- [240] Y. Hu, Y. Chen, J. Ma, J. Li, W. Huang, J. Chu, *Appl. Phys. Lett.* **2013**, *103*, 141112.
- [241] L. Yan, D. Yang, Q. Gong, Y. Li, *Micromachines* **2020**, *11*, 112.
- [242] D. Pan, B. Xu, S. Liu, J. Li, Y. Hu, D. Wu, J. Chu, *Opt. Lett.* **2020**, *45*, 2584.
- [243] D. Pan, S. Liu, J. Li, J. Ni, C. Xin, S. Ji, Z. Lao, C. Zhang, B. Xu, R. Li, S. Fan, P. Li, Y. Hu, D. Wu, J. Chu, *Adv. Funct. Mater.* **2022**, *32*, 2106917.
- [244] L. Liu, D. Yang, W. Wan, H. Yang, Q. Gong, Y. Li, *Nanophotonics* **2019**, *8*, 1087.
- [245] H. J. Levinson, T. A. Brunner, in *International Conference on Extreme Ultraviolet Lithography 2018* (Eds.: K. G. Ronse, P. A. Gargini, E. Hendrickx, P. P. Naulleau, T. Itani), SPIE, Bellingham, WA **2018**.
- [246] G. D. Hutcheson, in *Extreme Ultraviolet (EUV) Lithography IX* (Eds.: N. M. Felix, K. A. Goldberg), SPIE, Bellingham, WA **2018**.
- [247] M. Neisser, *J. Micro/Nanopatterning Mater. Metrol.* **2021**, *20*, 044601.



**Antonio Balena** graduated in Physics summa cum laude in 2017 and received his Ph.D. in Structures, Materials, and Nanotechnology Engineering from Università del Salento in May 2021. He worked as a postdoctoral fellow in the Istituto Italiano di Tecnologia, Center for Biomolecular Nanotechnologies (IIT@CBN) from June 2021 to November 2021. He then worked as PostDoc in Laboratoire Kastler Brossel in Paris Sorbonne University from December 2021 to October 2022 and as Researcher in IIT@CBN starting from October 2022. His research interests include micro and nanofabrication, quantum photonics, and neurophotonics.



**Marco Bianco** graduated in Physics summa cum laude in 2018 and worked as a Ph.D. student at Istituto Italiano di Tecnologia (IIT) from November 2018 to November 2021. In June 2022 he received his Ph.D. in Structures, Materials and Nanotechnology Engineering from Università del Salento. He is currently a postdoctoral fellow at IIT, Center for Biomolecular Nanotechnologies (IIT@CBN). His research interests include micro and nanofabrication, multifunctional neural interfaces, and two-photon lithography.



**Ferruccio Pisanello** is coordinator of the Multifunctional Neural Interfaces with deep brain regions research unit at the Istituto Italiano di Tecnologia Center for Biomolecular Nanotechnologies. He received the PhD degree in Physics at the University Pierre et Marie Curie (Paris) and his group strives at developing new paradigms to interface with the brain, exploiting physical phenomena in unconventional ways to realize a new generation of devices able to gather multifunctional signals from it and to control its physiology. He is the author of 62 publications in international peer-reviewed Journals, holder of 4 high-risk/high-gain competitive grants, and a member of SPIE Neurophotonics editorial board.



**Massimo De Vittorio** is Director of the Istituto Italiano di Tecnologia Center for Biomolecular Nanotechnologies in Lecce–Italy and Full Professor at Università del Salento. His research is currently focusing on new technologies for manipulating and recording brain activity and for skin sensors for IoMT (Internet of Medical Things) for monitoring and controlling health and wellness in real time. Author of about 400 manuscripts, 14 international patents, 10 book chapters, and more than 60 invited/keynote talks at international conferences; he is also senior editor of the Journal IEEE Transactions on Nanotechnology and cofounder of the international micro and nanoengineering society (iMNEs).